Examining the Effects of Mid Ocean Ridge Topography on 3D Marine Magnetometric Resistivity Model Responses

by

Lisa A. Lassner

B.S. Mathematics and Computer Science
Colorado School of Mines, 2001

Submitted in partial fulfillment for the requirements of the degree of

MASTERS OF SCIENCE
at the
MASSACHUSETTS INSTITUTE OF TECHNOLOGY
and
WOODS HOLE OCEANOGRAPHIC INSTITUTION
June, 2004

Signature of the Author .....
Joint Program in Oceanography/Applied Ocean Science and Engineering
Massachusetts Institute of Technology
and Woods Hole Oceanographic Institution
June, 2004

Certified by .....
Robert L. Evans
Thesis Supervisor

Accepted by .....
Greg Hirth
Chair, Joint Committee for Marine Geology and Geophysics
Massachusetts Institute of Technology/
Woods Hole Oceanographic Institution

Abstract

Methods which measure seafloor resistivity are uniquely suited to studying hydrothermal circulation in the crust. The magnetometric resistivity (MMR) technique is a galvanic method which uses a bipole current source with a magnetometer receiver. The resistivity of the subsurface can be estimated from the magnetic field read in MMR. In order to analyze and invert MMR data taken near Mid Ocean Ridges, it is important to understand the effects of ridge topography on MMR models. To analyze these effects a 3D MMR forward modeling program `MMR3D_fwd` is used to model Mid Ocean Ridges with varying slopes, resistivities, and source/receiver geometries. The modeled magnetic fields are compared with models with a flat seafloor to determine the impact of the ridge topography. Results show that for some of the ridges modeled, the effects of the topography were significant, suggesting that in some instances it is important to include ridge topography in forward models to obtain accurate results from data inversion.

Acknowledgements

I would like to thank my advisor Dr. Robert Evans for all of his help and support along the way. He has been instrumental in helping me with this work from providing the idea for the thesis work itself, to helping me create this document in the end, and everything in between. This was my first time writing a work like this and his patient guidance has been invaluable in this process.

I would like to also thank the members of my committee: Drs. Xavier Garcia and Stephane Rondenay of MIT. Their comments have helped shaped the direction of much of the analysis in this work.

Thanks also go out to Dr. Jiuping Chen from the University of British Columbia, Vancouver, for patiently answering questions in countless emails about the forward modeling code.

Lastly I would like to thank Aaron Newman and Shoshana Gourdin for reading and editing my thesis.

The work for this thesis has been supported by the Woods Hole Oceanographic Institution Academic Programs Fellowship, and the National Science Foundation Structure of the East Pacific Rise project.

Chapter 1

Introduction

The pattern of hydrothermal circulation near mid-ocean ridges can be studied by mapping temperature, salinity, porosity and permeability within the crust. To date, geophysical techniques have not been able to tightly constrain these parameters. Seismic methods, which are commonly used to map the structure of the crust at ridges, are sensitive to the closure of cracks due to hydrothermal alteration, but are insensitive to fluid temperature and salinity. Therefore, seismic techniques are ill-suited to mapping hydrothermal circulation. The resistivity of the crust is a strong function of both temperature and salinity as well as permeability and porosity. Methods which measure seafloor resistivity are therefore uniquely suited to studying hydrothermal circulation in the crust.

Seafloor resistivity is sensitive to the presence of seawater in the crust. This is because seawater has a very low resistivity compared to both air and crustal materials. Thus pore spaces filled with seawater will decrease the resistivity of the crust permitting more current to travel through the crust. High porosity structures will have more seawater filled space than those with low porosity which will generally result in a lower resistivity. However, the resistivity of the crust is also dependent on the interconnectedness of the pores. This means that a high porosity media could potentially be more resistive than one with low porosity if the pore space in the low porosity media is more effectively interconnected. While interconnectedness might intuitively be thought to be related to permeability, in practice quantitative links between resistivity and permeability are only poorly established.

The relationship between the porosity of a material and its resistivity is often

described by the empirical relationship known as Archie's Law:

$$\frac{\rho_m}{\rho_f} = \phi^{-t} \tag{1.1}$$

where ρ_m is the resistivity of the material, ρ_f is the resistivity of the fluid in the pore, ϕ is the porosity fraction and t is an experimentally derived parameter which varies between 1.2 and 3 [Archie, 1942]. The resistivity of the seafloor is thus also dependent on the resistivity of the pore fluid, or the resistivity of the seawater. The resistivity of seawater is a function of temperature, ranging from values of $0.3\Omega m$ for deep seawater at 2^o C, to $0.04\Omega m$ for seawater at 350^o C. For temperatures up to 300^o C the conductivity (reciprocal of resistivity) can be estimated by

$$\sigma = 3 + T/10 \tag{1.2}$$

[Von Herzen et al., 1983]. Representative values for resistivities in the marine environment are summarized in Figure 1-1.

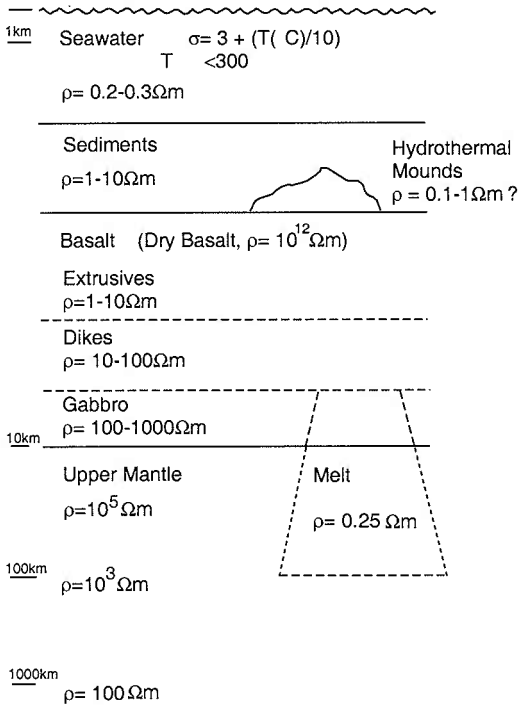

Figure 1-1: *Resistivity values for structures in the marine environment.*

The magnetometric resistivity (MMR) technique is a galvanic method which uses a bipole current source with a magnetometer receiver. If the transmitted current is

known, the resistivity of the seafloor can be estimated from the measured magnetic field strength. Marine MMR uses a source with one electrode on the seafloor and one near the seasurface, with the magnetometer on the seafloor a distance **r** away from the source (figure 1-2). The magnetometer receiver used in the MMR method reads low-level magnetic fields (on the order of 100 pT) which are also low-frequency (1-5 Hz). Most of the current has a return path through the seawater, but some of it penetrates the seafloor and the field generated by that current provides information about resistivity structure below the seafloor.

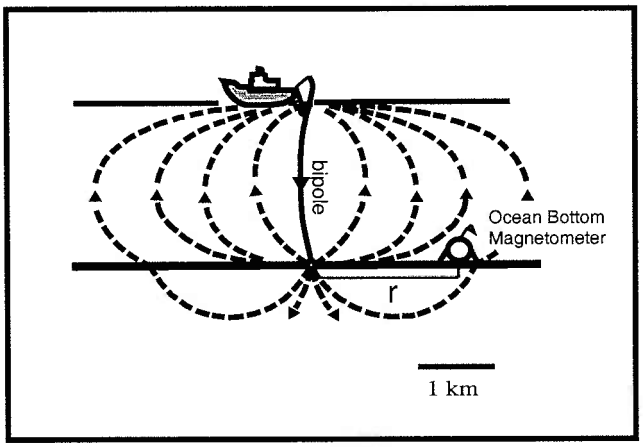

Figure 1-2: *MOSES MMR setup*

The magnetic field recorded at the magnetometer is a superposition of two fields: the first is the field from the wire connecting the two electrodes, the second is the field from the penetration of the current into the seafloor. In the rest of this thesis the combination of the two fields is referred to as the *total* field and the field from the seafloor is referred to as the *anomalous* field. Because the field from the wire will be constant, the anomalous field can be derived from the total field by subtracting the field from the wire.

Field Comparison			
Factors	Anomalous	Wire	Total
current source	crust	wire	crust + wire
sign	negative	positive	positive
magnitude	medium	large	small

MMR overcomes two problems that make other galvanic methods impractical for surveying the oceanic crust. Other methods which measure the DC electric field are

difficult to use in the marine environment because they often require large bipole separations (several times the depth of the sea layer) to resolve the resistivity of the sea floor. These techniques are sensitive to even small superficial inhomogeneities in the surface layer, where the buildup of charge on the boundaries can cause the data to be very noisy. MMR can resolve features in the crust with bipole separations the size of the sea layer depth, and because the magnetic field is an integral over a volume distribution of current, MMR data is less sensitive to heterogeneities in surface resistivity than other galvanic techniques.

The MMR method for terrestrial use was first patented by Jakovsky in 1933 but was then largely ignored until further developments were made by [Edwards, 1974]. Edwards modified the MMR technique for marine use in 1981. He developed 1D analytical models for the marine MMR technique in the presence of both layered and halfspace models (these models provide the basis for the model discussed in chapter 2). The results of these models showed that the presence of thin conductive or resistive layers could be detected using the MMR response. The modeling also explored the effect of source frequency on the data. These models show that the magnetic field is largely independent of frequency with small frequency effects at large source to receiver distances [Edwards et al., 1981]. Edwards also studied the effects of macroanisotropy (a grouping of thin isotropic layers of varying resistivities) on MMR results. At high frequencies, in the presence of induction in the seawater, the coefficient of anisotropy can be calculated. To determine the apparent anisotropies in these conditions, Edwards developed methods for calculating apparent resistivities and apparent anisotropies [Edwards et al., 1984].

The first marine MMR experiment was conducted by Edwards et al. [1985]. This sea test determined the sea sediment thickness and conductivity at Bute Inlet in British Columbia. The experiment used one receiver with two horizontal orthogonal magnetometers. The receiver was placed in one location and remained stationary while the source was excited at 16 stations along the axis of the valley to either side of the receiver with source to receiver distances ranging between 150 m to 2 km. Apparent resistivities calculated from the data show a systematic error between the stations on either sides of the receiver. One dimensional inversions of the data produced a model with a layer of sediment over a half-space with a layer resistivity and thickness of $1.9\Omega m$ and 560 m respectively. The resistivity estimate corresponded well with measurements of porosity from core samples, and the thickness was below the bound of estimated thickness obtained through

extrapolation of seafloor topography.

Nobes et al. [1986] conducted an MMR experiment in Middle Valley on the Juan de Fuca Ridge, a sedimented basin with known hydrothermal vent fields. The study explored 2 sites with 2 receiver stations used at each site. The transmitter was excited at 11 stations with source to receiver distances ranging from 600 to 6200 m. At the second site the transmitter was excited at 20 different locations creating source to receiver distances of 400 to 4000 m. One-dimensional inversions of the data show a sediment layer thickness of 1800 ± 300 m with a resistivity of $0.82 \pm 0.06 \Omega m$. Estimates of the porosity of the sediments were calculated by correcting the pore-fluid resistivity using basement temperatures determined by previous studies. The estimated porosity values showed good agreement with DSDP hole 504B porosity values and with estimates of porosity from seismic data. The study concluded that the permeabilities in the basalts were large enough to allow hydrothermal circulation to occur in this area.

Another study was performed at the Juan de Fuca Ridge in the Middle Valley by Wolfgram et al. [1984]. This experiment was a field test of an induction coil receiver in place of the commonly used flux-gate magnetometer for the MMR method. The setup for the experiment is referred to as MINI-MOSES (MOSES is an acronym standing for magnetometric offshore electrical sounding). This technique was developed to study polymetallic sulfide deposits in very localized areas on the seafloor. In this experimental setup both the source to receiver distances and the bipole lengths are much smaller than in conventional MMR studies. The experiment only collected data at 2 receiver stations with source to receiver distances of 30 and 100 m and bipole lengths of 100 m. The study did not obtain enough data to draw conclusions about the study area but showed that this type of experimental setup is feasible for MMR studies.

Nobes et al. [1992] conducted another study in the Middle Valley in 1992 in an area with evidence of hydrothermal activity to try to determine the extent of mineralization in the area and to provide constraints on temperatures in the crust. The source was excited near a mound along North-South and East-West trending lines. Two receivers were used in each of 3 deployments. The regional data were fit with a layered model with a sediment layer overlying the basement. The data near the hydrothermal mound was best fit by a three layer model with a mound overlying a sediment layer. A nearby heat anomaly had a large effect on this data. Nobes et al. suggested that the anomaly may be a 2D or 3D feature even though

the data can be fit by simple 1D models.

In 1998, Evans conducted an MMR survey of the Cleft-Vance overlapping spreading center on the Juan de Fuca Ridge in an attempt to map the extent of hydrothermal circulation at this site [Evans et al., 1998]. Three magnetometers collected magnetic field data, one on the neovolcanic zone (NVZ) of the northern Cleft segment, one northeast of the NVZ near a pillow flow, and one off the NVZ. The bipole source was excited at 34 transmission stations, most of which were placed on a line parallel to strike or one across strike with source to receiver distances of up to 5 km. The depth of penetration of the current was approximately 1 km. The data collected varied in amplitude from receiver to receiver. This variation was determined to be a result of the three dimensionality of the seafloor resistivity structure. Because only one of the three magnetometers was placed on top of the conductive body, it produced a very different response compared to the other two, showing the effects of the buried conductor on the magnetic field. This study defined two zones of low resistivity ($1\Omega m$), which coincided with the NVZs of the Cleft and Vance segments, and were determined to be the result of hot seawater percolating through the upper crust. Evans et al. used forward modeling to try to account for the low resistivities observed in the study. The model which best explains the data has two conductive bodies within the top 1 km of the crust underneath the NVZs of both segments. The data constrained the northern extent of the Cleft anomaly but not of the Vance. The results of the study were consistent with hydrothermal circulation models and in the case of the anomaly at the Cleft segment, observations from submersible and camera tows. Evans et al. determined that in order to develop a better constraints on the pattern of hydrothermal circulation, more magnetometers were needed to provide better coverage of the survey area.

A similar study was conducted between the Clipperton and Siquieros transform faults at 9°50'N on the East Pacific Rise (EPR) [Evans et al., 2002]. This region is known to be underlain by a 500 m wide melt body that extends beneath most of the ridge at a depth of 1.5 km, continuous along strike [Detrick et al., 1987]. An eruption of this segment in 1991 caused an increase in hydrothermal venting near the neovolcanic zone. The study used 10 magnetometers and 200 transmission stations, with source to receiver distances up to 5 km, most on lines parallel to strike and although some were on three lines that crossed strike. The magnetometers were placed both on sites of with and without known hydrothermal activity. Data from this survey showed low apparent resistivities on-axis which is

consistent with zones of high temperature pore fluids associated with hydrothermal circulation. Receivers at sites along the axis, both those near areas of known venting and those placed in areas with no hydrothermal activity recorded higher amplitude magnetic fields with little variability between receivers. The uniformity of the data regardless of position along the axis, suggests the presence of a 2D thermal structure with a size of at least 100 m. One-Dimensional inversions were conducted on the data on and off-axis. The resistivity profiles derived from the inversions do not support the theory of areas of broad upwelling below the ridges, rather they suggest that venting is due to pore fluids moving through fractures with dimensions on the order of tens of meters. At depths greater than 1 km, the resistivity profiles from the on and off-axis receivers are similar which suggests that the temperatures at this depth are also similar at these sites. This observation may constrain the depth of hydrothermal circulation at the ridge. Evans et al. determined that 3D inversions of the data were needed to provide a better picture of the 3D resistivity structure of the ridge and the effects of hydrothermal circulation on that structure.

The effects of terrain on 3D terrestrial MMR models has been explored by Oppliger, [1984]. His work used an integral equation method to estimate the effects of topography and established that topography can have a large effect on MMR data. He also developed a method of calculating a terrain correction. To calculate the correction a model of the survey location is calculated with the subsurface consisting of a homogeneous half-space. These models include the terrain of the area. Then the terrain modeled data is subtracted from the field collected data to remove the effects of the topography.

Yang and Tseng, 1992, have also examined the effects of topography on land MMR models. Their study was aimed at developing a method to remove the effects of the topography. They used 2D models generated using a finite-element method and provided some results for models of a trapezoidal hill, a ramp, and a trapezoidal valley [Yang and Tseng, 1992].

While both Oppliger and Yang and Tseng have demonstrated that topography can have an effect on land based MMR models, there remains no good rule of thumb to determine when the effect of the topography becomes large enough to be an important consideration in inverting data. Most importantly there has been no published treatment of the effects of topography on marine based MMR. 3D inversions of MMR data are computationally expensive, and including realistic topography in MMR models is at this time very difficult. If the effects of certain

topographies on MMR models are negligible then much effort can be saved by neglecting the topography in forward models for the purposes of inversion. Whether or not the topography of the ridge is important to include in the model for the purposes of 3D inversion therefore remains an important question. This thesis will examine the impact of ridge topography on MMR models and try to answer the question of whether or not this topography needs to be included in the 3D inversions of the data from the East Pacific Rise [Evans et al., 2002].

Chapter 2

1D Model

To provide an understanding of the physics of the MMR method, a 1D model of a layered earth is developed below. In this model the resistivity of the earth varies only with depth. This model is suitable for calculating the magnetic field response from both an homogeneous half-space and a layered section of internally homogeneous layers. It also forms the basis for the 1D MMR modeling code discussed in this thesis. In chapter 3 I compare the results of the magnetic fields calculated by both the 3D and the 1D code for these models to assess the accuracy of the results of the 3D modeling code.

The magnetic field due to a constant current source is defined by Ampere's Law:

$$\nabla \times \mathbf{B} = \mu_o \mathbf{J} = \mu_o \sigma \mathbf{E}. \tag{2.1}$$

Where $\mathbf{B}$ is the magnetic field, $\mathbf{J}$ is the current density and $\mathbf{E}$ is the electric field. Ampere's law can be written in integral closed circuit form

$$\oint \mathbf{B}.dl = \mu_o \mathbf{I}, \tag{2.2}$$

which states that a magnetic field through a closed circuit is proportional to the current $\mathbf{I}$ passing through it. The azimuthal component of this field is constant around the Ampere circuit, and is proportional to the current entering the seafloor through the circuit. If the field is recorded at a magnetometer a distance r from the source, then that field is due to the current entering the seafloor within a circle of radius $\mathbf{r}$ (figure 2-1).
Other galvanic techniques use a DC or static approximation. In order to provide a

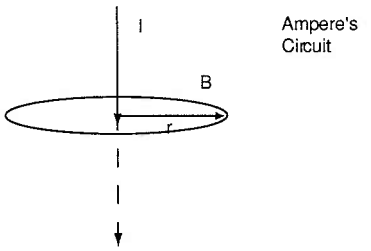

Figure 2-1: *Plan view of Ampere's Circuit, current source* $\boldsymbol{I}$ *passes through the circuit in the center*

basis of comparison between this and other techniques it is therefore useful to make a DC or static approximation. Taking the curl of eqn 2.1

$$\nabla\times\nabla\times\mathbf{B} = \mu_o\nabla\times(\sigma\mathbf{E}) \tag{2.3}$$

$$= \mu_o\{\nabla\sigma\times\mathbf{E}+\sigma\nabla\times\mathbf{E}\} \tag{2.4}$$

and removing the $\sigma\nabla\times\mathbf{E}$ term, which is zero due to the static approximation, yields

$$\nabla\times\nabla\times\mathbf{B} = \mu_o\nabla\sigma\times\mathbf{E}. \tag{2.5}$$

Rewriting this in cylindrical coordinates we obtain:

$$\frac{\partial^2\mathbf{B}}{\partial r^2}+\frac{1}{r}\frac{\partial\mathbf{B}}{\partial r}-\frac{\mathbf{B}}{r^2}-\frac{1}{\sigma}\frac{\partial\sigma}{\partial z}\frac{\partial\mathbf{B}}{\partial z}+\frac{\partial^2\mathbf{B}}{\partial z^2}=0. \tag{2.6}$$

Using resistivity $\rho=\frac{1}{\sigma}$ this can also be written as:

$$\frac{\partial^2\mathbf{B}}{\partial r^2}+\frac{1}{r}\frac{\partial\mathbf{B}}{\partial r}-\frac{\mathbf{B}}{r^2}+\frac{1}{\rho}\frac{\partial\rho}{\partial z}\frac{\partial\mathbf{B}}{\partial z}+\frac{\partial^2\mathbf{B}}{\partial z^2}=0 \tag{2.7}$$

To simplify the mathematics a Hankel transform of the form

$$\bar{F}(p,q)=\bar{F}(\lambda)=2\pi\int_0^\infty rF(r)J_o(\lambda r)dr \tag{2.8}$$

is applied to eqn 2.7

$$\frac{\partial^2\mathbf{B}}{\partial r^2}+\frac{1}{r}\frac{\partial\mathbf{B}}{\partial r}-\frac{\mathbf{B}}{r^2} = \left[\frac{\partial^2}{\partial r^2}+\frac{1}{r}\frac{\partial}{\partial r}-\frac{1}{r^2}\right]\int_0^\infty\lambda\bar{\mathbf{B}}(\lambda)J_1(\lambda r)d\lambda \tag{2.9}$$

$$= \int_0^\infty\lambda\bar{\mathbf{B}}(\lambda)\left[\frac{\partial^2J_1(\lambda r)}{\partial r^2}+\frac{1}{r}\frac{\partial J_1(\lambda r)}{\partial r}-\frac{J_1(\lambda r)}{r^2}\right]d\lambda. \tag{2.10}$$

The orthogonality property of Bessel functions leads to

$$\frac{\partial^2 \bar{\mathbf{B}}}{\partial z^2} + \frac{1}{\rho}\frac{\partial \rho}{\partial z}\frac{\partial \bar{\mathbf{B}}}{\partial z} - \lambda^2 \bar{\mathbf{B}} = 0 \tag{2.11}$$

in the Hankel domain.

Let us define a layered model consisting of N layers with a watercolumn depth of D. The seawater/seafloor interface is defined as $Z = 0$ and the seawater/air interface is defined as $Z = -D$. The first layer below the seafloor is defined as layer 1, with the layer numbers increasing downward to layer N. Each layer has a uniform resistivity ρ_i. The depth of the upper interface is defined as $z = d_i$ and the depth of the lower interface is defined as $z = d_{i+1}$. The source electrodes are placed at $Z = 0$ and $Z = -D$ and connected by a wire which carries a current I. The azimuthal field due to this source is calculated as a function of r, the distance to the magnetometer, and the resistivity structure of the subsurface. A half-space solution can be calculated from this layered model by making $N = 1$ (figure 2-2). Within a layer of uniform resistivity ($\frac{\partial \rho}{\partial z} = 0$) eqn 2.11 becomes

$$\frac{\partial^2 \bar{\mathbf{B}}}{\partial z^2} = -\lambda^2 \bar{\mathbf{B}} \tag{2.12}$$

Eqn 2.12 has solutions of the form:

$$\bar{\mathbf{B}}(\lambda, z) = [Ue^{(-\lambda z)} + Ve^{(\lambda z)}]$$

or

$$\bar{\mathbf{B}}(\lambda, z) = [U\cosh(\lambda z) + V\sinh(\lambda z)].$$

By Ampere's Law the solution near the source is

$$\mathbf{B}(r) = \frac{\mu_o I}{2\pi r} \tag{2.13}$$

or

$$\bar{\mathbf{B}}(\lambda) = \frac{\mu_o I}{2\pi\lambda}$$

in the Hankel domain.

Ampere's law as a function of depth for the azimuthal component of the magnetic

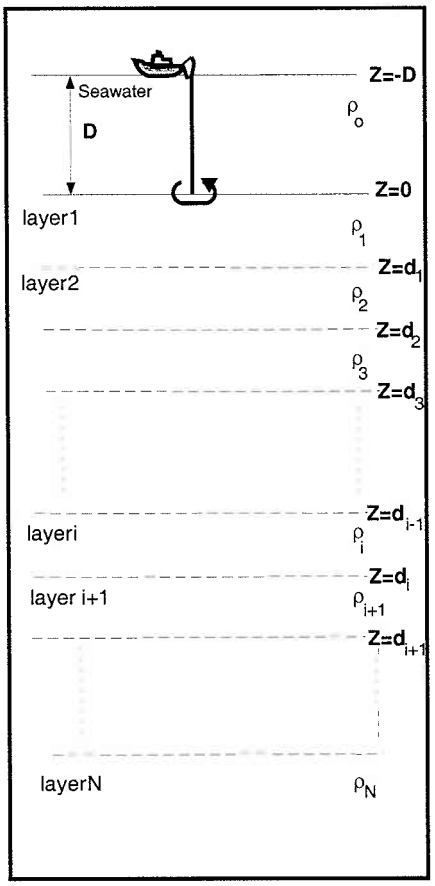

Figure 2-2: *Model Layout*

field only yields:

$$\mu_o \sigma \mathbf{E}_r = -\frac{\partial \mathbf{B}_\phi}{\partial z}.$$

Replacing $\mathbf{B}$ with its solution above we obtain:

$$\mu_o \bar{\mathbf{E}}_r = -\lambda\rho \left[U \sinh(\lambda z) + V \cosh(\lambda z)\right].$$

To simplify the mathematics Q is defined as

$$Q(\lambda, z) = \frac{\bar{\mathbf{B}}(\lambda, z)}{\mu_o \bar{\mathbf{E}}_r(\lambda, z)} \tag{2.14}$$

$$= \frac{-1}{\lambda\rho}\left[\frac{U\cosh(\lambda z) + V\sinh(\lambda z)}{U\sinh(\lambda z) + V\cosh(\lambda z)}\right] \tag{2.15}$$

. Dividing the right hand side by $V\cosh(\lambda z)$, Q is now defined by:

$$Q = \frac{-1}{\lambda\rho}\left[\frac{\frac{U}{V}+\tanh(\lambda z)}{\frac{U}{V}\tanh(\lambda z)+1}\right]. \tag{2.16}$$

A recursive scheme is derived for Q for each layer

$$Q_i = \frac{-1}{\lambda\rho_i}\left[\frac{\frac{U}{V}+\tanh(-\lambda d_i)}{1+\frac{U}{V}\tanh(-\lambda d_i)}\right] \tag{2.17}$$

$$= \frac{1}{\lambda\rho_i}\left[\frac{\frac{-U}{V}+\tanh(\lambda d_i)}{1-\frac{U}{V}\tanh(\lambda d_i)}\right] \tag{2.18}$$

$$Q_{i+1} = \frac{-1}{\lambda\rho_i}\left[\frac{U}{V}\right]. \tag{2.19}$$

Thus Q_i can be written in terms of Q_{i+1}

$$Q_i = \frac{1}{\lambda\rho_i}\left[\frac{\lambda\rho_i Q_{i+1}+\tanh(\lambda d_i)}{1+\lambda\rho_i Q_{i+1}\tanh(\lambda d_i)}\right] \tag{2.20}$$

and

$$Q_n = \frac{1}{\lambda\rho_n} \tag{2.21}$$

for the final layer which is an infinite half-space whose bottom interface is at $z=\infty$.

Therefore starting with the Nth layer the value for Q at the $z=0$ can be calculated using the recursion relationship where

$$Q_0 = \frac{\bar{\mathbf{B}}(\lambda,0)}{\mu_o\bar{\mathbf{E}}_r(\lambda,0)}.$$

To determine $\mathbf{B}$ the exponential solution to eqn 2.11 is used superimposed on the solution for $\mathbf{B}$ near the source.

$$\bar{\mathbf{B}}^{ocean}(\lambda,z) = \frac{\mu_o I}{2\pi}(Fe^{(-\lambda z)}+Ge^{(\lambda z)}+\frac{1}{\lambda}) \tag{2.22}$$

Because the magnetic field is due to the flow of current and no current flows across the seasurface $\bar{\mathbf{B}}(\lambda,D)=0$ and

$$Fe^{\lambda D}+Ge^{-\lambda D} = -\frac{1}{\lambda}$$

Taking the derivative and evaluating at the seafloor

$$\mu_o \mathbf{E}_r(\lambda, 0) = \frac{\mu_o I \rho_0}{2\pi}(-\lambda F + \lambda G) \tag{2.23}$$

By definition the ratio of $\frac{\bar{\mathbf{B}}_{(\lambda,0)}}{\mu_0 \bar{\mathbf{E}}_{(\lambda,0)}}$ must be equal to Q_0 evaluated through the recursion relationship.

F and G may be removed from the solution through algebraic manipulation. Taking the inverse Hankel transform

$$\mathbf{B}(r, 0) = \frac{\mu_o I}{2\pi} \int_0^\infty (\frac{1-\kappa}{2}) \frac{[1 - 2e^{-\lambda D} + e^{-2\lambda D}]}{[1 - \kappa e^{-2\lambda D}]} J_1(\lambda r) d\lambda. \tag{2.24}$$

With κ defined as

$$\kappa = \frac{1 - \rho_0 \lambda Q_0}{1 + \rho_0 \lambda Q_0}$$

This solution is dependent only on the current of the source **I**, the source to magnetometer distance in plan view r, the parameters which define the geometry of the layers, and their resistivities.

Therefore in order to solve for the magnetic field at the seafloor due to any layer geometry Q_0 is defined using eqns 2.20 and 2.21. Then Q_0 is substituted into the expression for κ in eqn 2.24.

Thus the solution of the magnetic field due to the current flowing into a halfspace of resistivity ρ_c is

$$\mathbf{B}(r, 0) = \frac{\mu_o I}{2\pi} \int_0^\infty \frac{1-\kappa}{2} J_1(\lambda r) d\lambda \tag{2.25}$$

with

$$\kappa = \frac{\rho_c - \rho_0}{\rho_c + \rho_0}$$

yielding

$$\mathbf{B}(r, 0) = \frac{\mu_o I}{2\pi r} \Big(\frac{\rho_o}{\rho_c + \rho_o} \Big). \tag{2.26}$$

Because the half-space model is simply the layered model with only one layer, this result only depends on the resistivity contrast between the seawater and the seafloor, the distance r, and the source current I. Responses from a uniform half-space are calculated for half-space resistivities of 1, 10, 15 and $100 \Omega m$. Because a highly resistive half-space will allow less penetration of current, the resulting

magnetic field decreases in strength with increasing resistivity (figure 2-3).

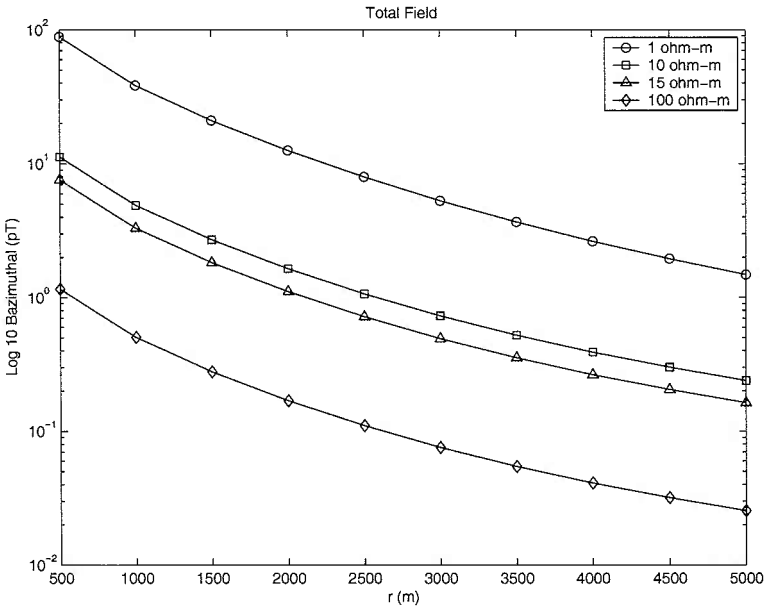

Figure 2-3: *Magnetic field responses to a homogeneous half-space of varying resistivity.*

Chapter 3

Forward Model Code Evaluation and Modeling Tests

The modeling described in this thesis was done with the program `MMR3D_fwd`, from Doug Oldenburg's group at University of British Columbia, Vancouver [Chen et al., 2002]. `MMR3D_fwd` is a Matlab program which generates the anomalous magnetic field response from a 3D model defined by a data file. The 3D models are defined by the number of cells in each dimension, the size of each cell, the distribution of cell above and below the seafloor, and the resistivity of each cell. The distribution of cells in the model is called a mesh. There are limitations on the mesh size due to a memory limitation inherent in Matlab which restrict Matlab programs to only 2 GB of RAM. The largest mesh that I have been able to run is 68 x 68 x 40 cells.

Topography of the seawater/seafloor interface is also defined in the data file. No topography was applied to the models in this chapter.

Four model types are explored in this work. The first three - homogeneous half-space, a buried layer, and a buried anomaly - are discussed in this chapter. The effect of topography on the homogeneous half-space is discussed in the fourth chapter.

3.1 Models

3.1.1 Homogeneous half-space models

The magnetic field resulting from an homogeneous half-space was calculated for half-spaces of varying resistivities. Because the homogeneous half-space model is a 1D model, the results from the 3D models are compared to those calculated by a 1D modeling code. I evaluated several different meshes to try to develop the smallest mesh for the homogeneous half-space model calculated by the 3D code that would also minimize the root mean square error (RMSE) between the 1D and 3D forward models. I compared the results from these meshes to the 1D half-space model with a resistivity of $10\Omega m$. The best mesh for this model was 66 cells long in the x and y directions and 40 in the z direction. The cell spacing in the x and y directions are identical so I include a figure showing the mesh in the x-z plane. This mesh has finer mesh spacing near the center of the survey area and at the seawater/seafloor interface (Figure 3-1). In order to obtain good results the mesh needs to be symmetric about the center in both the x and y directions The RMSE between the 3D solution using the best mesh and the 1D solution was 1.44 pT. I also calculated

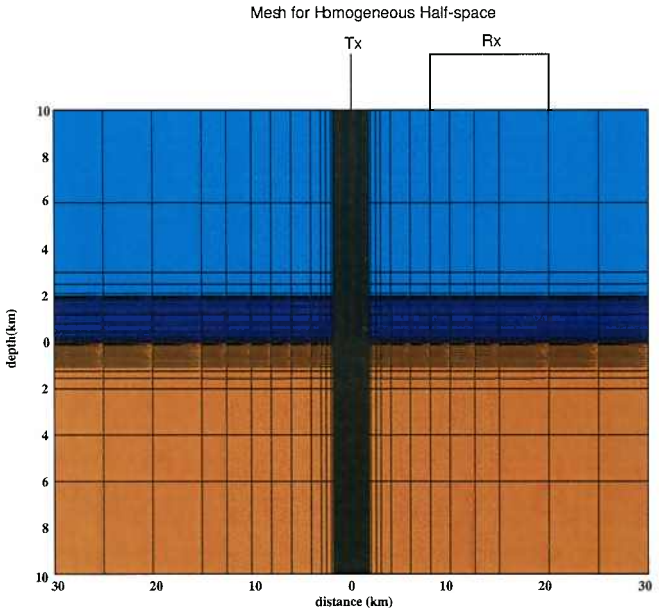

Figure 3-1: *Mesh for homogeneous half-space models, shown in x-z plane where the x axis is distance and the z axis is depth. Light blue cells are air, dark blue cells are water, and brown cells are below the seafloor*

the RMSE and relative RMSE between the 3D model solution and the 1D model solution for half-spaces with resistivities of 1, 5, 8, 10, 15, 50, 75 and 100Ωm. The RMSE increases with increasing resistivity but seems to level off such that half-spaces with resistivities of 15Ωm and higher have similar RMSEs (Figure 3-2). However, the relative RMSEs increase with increasing resistivity without leveling off (Figure 3-3). This shows that independent of the amplitude of the magnetic fields, the more resistive the half-space the larger the error between the 1D and 3D models.

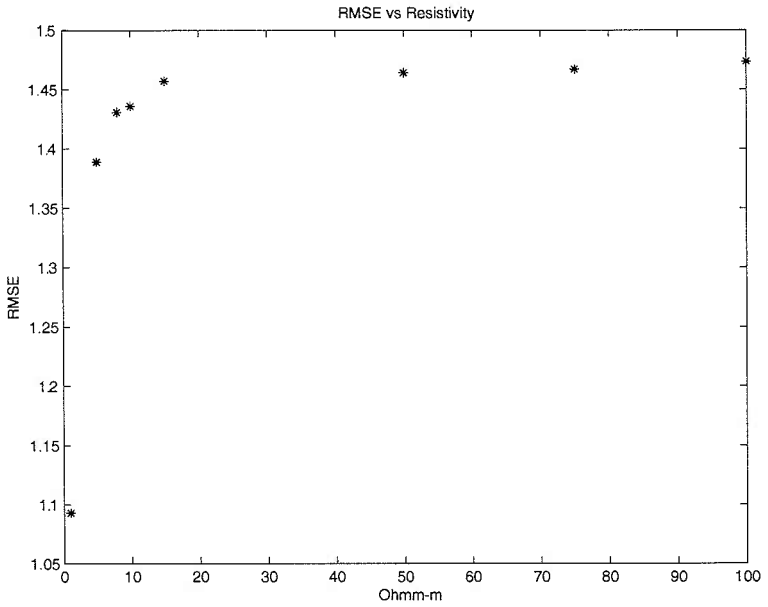

Figure 3-2: *RMSE of homogeneous half-space models for varying resistivities*

3.1.2 Layered Model

The next model I produced is a model with one layer against an homogeneous background. This is a good model for use in evaluating the 3D code because it is essentially 1D, in that the resistivity only varies in the z-direction. I used a background resistivity of 10Ωm and a layer resistivity of 1Ωm. Using the best mesh for the homogeneous half-space model gave a high RMSE of 4.98 between the 1D and 3D models. I created a new mesh for use with layered models with smaller cells near the interface, which was 66 cells in the x and y directions and 44 in the z-direction. The mesh was once again identical in the x and y direction and is shown in the x-z plane (figure 3-4). This model was compared with a 1D model with the same resistive layer. The resulting RMSE was 2.03 pT. Figure 3-5 shows

the 1D and 3D anomalous fields. The 3D layered model seems to be a good approximation of the 1D layered model for source to receiver distances larger than 2500 m. The largest errors are in the receivers close to the source; this is likely due to mesh effects. Because the mesh size is in part controlled by the Matlab memory limitation, further fining near the source is not possible. This is likely the cause of larger errors near the source.

3.1.3 3D Anomaly

The final model I created was a 3D anomaly in the shape of a cube. I used the same mesh that was used for the layered model for these models (Figure 3-6). To determine the effects of the anomaly on the magnetic fields I compared the fields with those from a homogenous half-space with the same resistivity as the background from the anomaly model. To determine the effect of the anomaly on the magnetic fields the relative RMSE was calculated:

$$relRMSE = \sqrt{\frac{1}{n}\sum_{i=1}^{n}\left(\frac{anom(i)}{hhs(i)} - 1\right)^2} \tag{3.1}$$

where **n** is the number of receivers, **anom** is the magnetic field due to the model with the anomaly, and **hhs** is the magnetic field due to an homogeneous half-space. The relative RMSE is used because I believe it is more robust than the regular RMSE. Indeed, the relative RMSE cancels some of the noise in the anomalous field by dividing by a field with similar errors due to meshing.

To observe the effects of the anomaly on the fields I varied several different parameters: the depth of the anomaly, lateral distance of the anomaly from the source, the size of the anomaly and the resistivity contrast between the anomaly and the background resistivity of the subsurface. To examine the effects on depth and lateral distance from the source I used an anomaly of $0.303\Omega m$ (the resistivity of seawater) measuring 0.5 km^3. The anomalies with varying depth were centered at the source, and the anomalies with varying lateral distance were placed at 500 m depth.

The further the anomaly is from the source, the less effect it should have on the magnetic fields produced by the model, because less current passes through the anomaly. Therefore, the magnetic fields for anomalies with increasing depth should

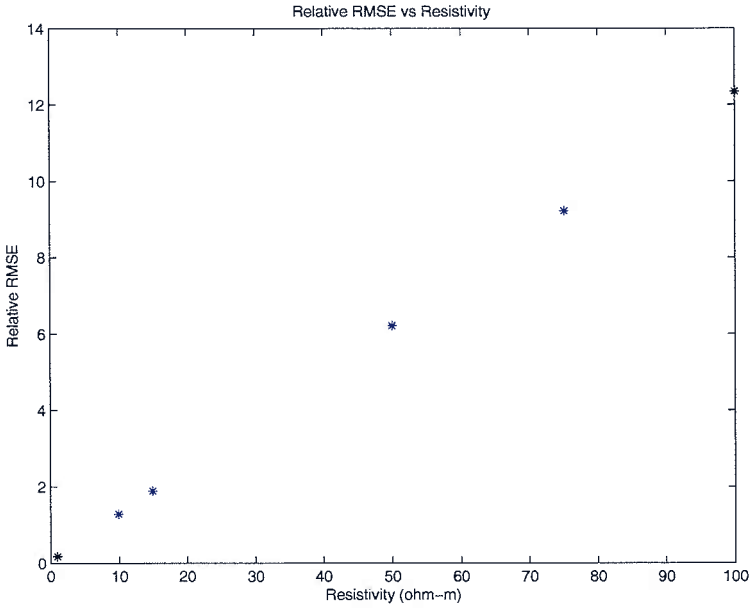

Figure 3-3: *Relative RMSE of homogeneous half-space models for varying resistivities*

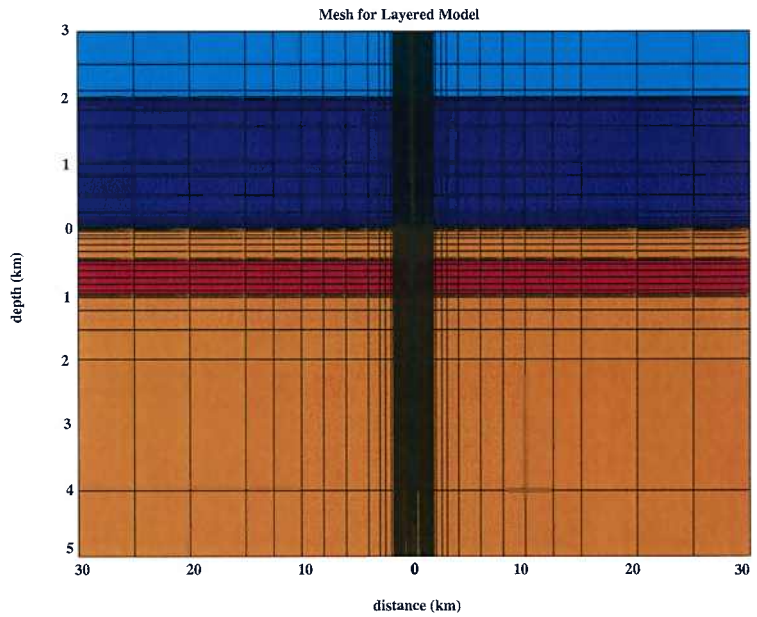

Figure 3-4: *Mesh for layered models, shown in x-z plane where the x axis is distance and the z axis is depth. Light blue cells are air, dark blue cells are water, brown cells are below the seafloor, and red cells are the layer.*

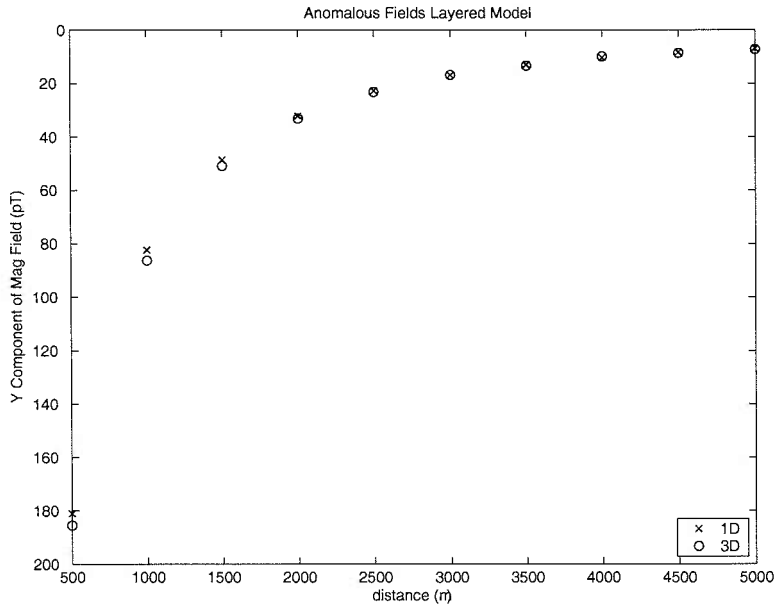

Figure 3-5: *Anomalous magnetic fields for the 3D and 1D layered models.*

approach the magnetic fields from a homogeneous half-space (figure 3-7). In the case of lateral distance from the source the anomaly is moved further away from the actual source but closer to some of the receivers (figure 3-8). The variability in the relative RMSEs seems to be due to noise in this case as the fields are almost indistinguishable from each other.

The relative RMSE should increase with an increase in size of the anomaly. The larger the anomaly, the larger the area of higher conductivity subsurface, and the more current paths can pass through it, yielding a larger response in the magnetic field (figure 3-9). Finally, the relative RMSE also decreases with increasing resistivity. The more resistive the anomaly the closer it approaches to the background resistivity of the model and therefore the smaller its effect (figure 3-10).

3.2 Apparent Resistivity

A common way to look at results from MMR models is to look at the apparent resistivities which can be calculated from the model's magnetic fields. Some attempts were made to make these kinds of figures. The first stab at calculating the apparent resistivities was to use an apparent resistivity formula derived by Jiuping

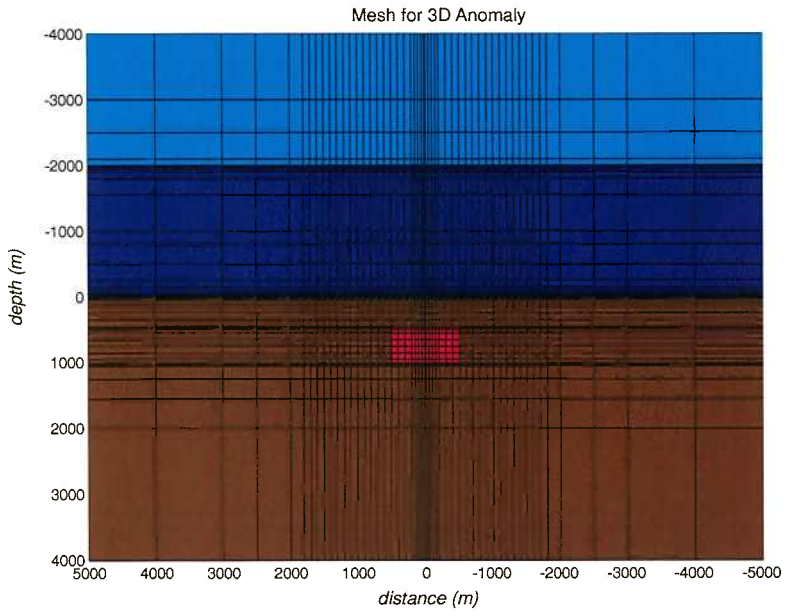

Figure 3-6: *Mesh for 3D anomaly models, shown in xz plane where the x axis is distance and the z axis is depth. Light blue cells are air, dark blue cells are water, brown cells are below the seafloor, and red cells are the resistivity anomaly.*

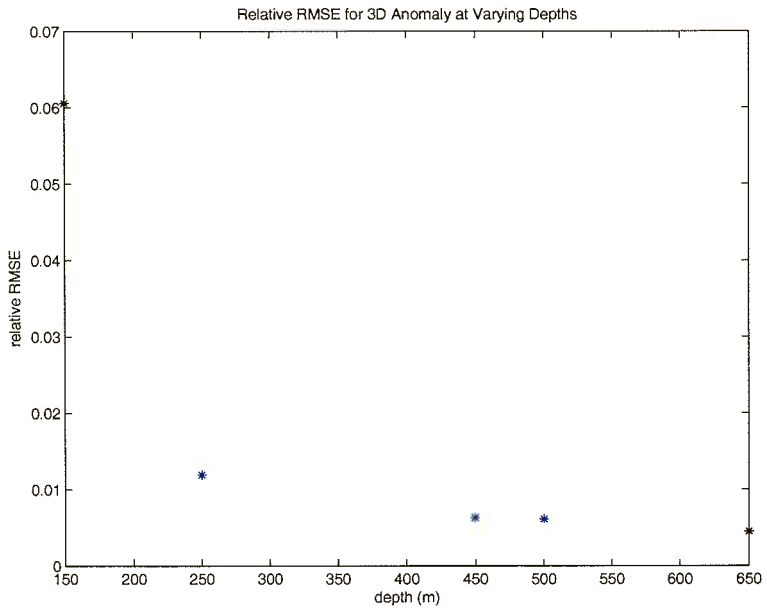

Figure 3-7: *Relative RMSEs for a* $0.303\Omega m$ *anomaly of 0.5* km^3 *against a background of* $30\Omega m$ *at depths of 150, 250, 450, 650 and 1050 m.*

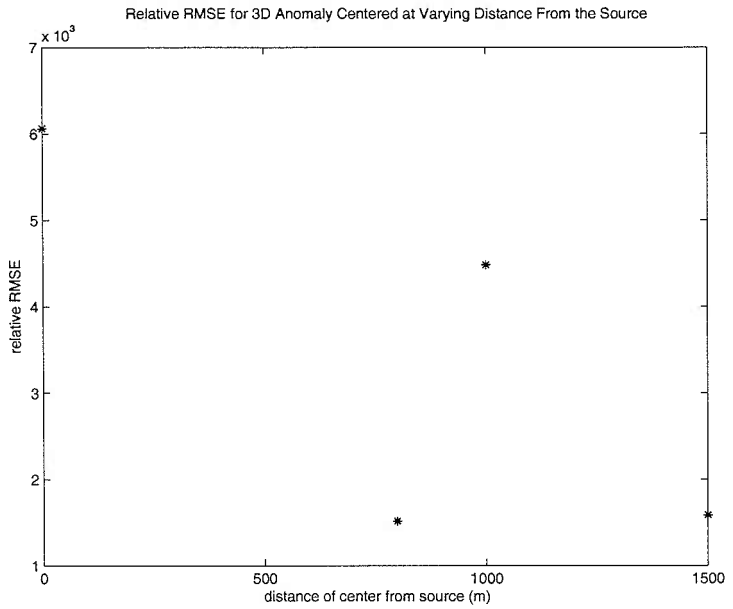

Figure 3-8: *Relative RMSEs for a* $0.303\Omega m$ *anomaly of 0.5* km^3 *against a background of* $30\Omega m$ *centered at a lateral distance from the source of 0, 300, 500, 1000 and 1500 m.*

Chen. This formula, like those by [Chave et al., 1991] and [Wolfgram et al., 1986], uses the *total* magnetic field, which is the field which is read by the magnetometer receiver. The formulas from Chave, Wolfgram and Chen are shown below.

$$\rho_a = \frac{\mu_0 I H \rho_0}{4\pi R^2 B_\phi} \tag{3.2}$$

$$\rho_a = \frac{\mu_0 I \rho_0}{2\pi R B_\phi} \frac{H}{\sqrt{H^2 + R^2}} - \rho_0 \tag{3.3}$$

$$\rho_a = \frac{\mu_0 I}{2\pi R} \frac{\rho_0}{B_\phi} \left[\frac{1.5}{\sqrt{1 + (R/H)^2}} - \frac{\alpha}{\sqrt{1 + [R/(2H)]^2}} \right] - \rho_0 \tag{3.4}$$

where

$$\alpha = \begin{cases} 0.5 & \text{if } R/H < 0.9 \\ 0.1333 R/H + 0.38 & \text{if } 0.9 \leq R/H \leq 1.2 \\ 0.54 & \text{if } R/H > 1.2 \end{cases}$$

Because the modeling code outputs the *anomalous* magnetic field, the *total* field

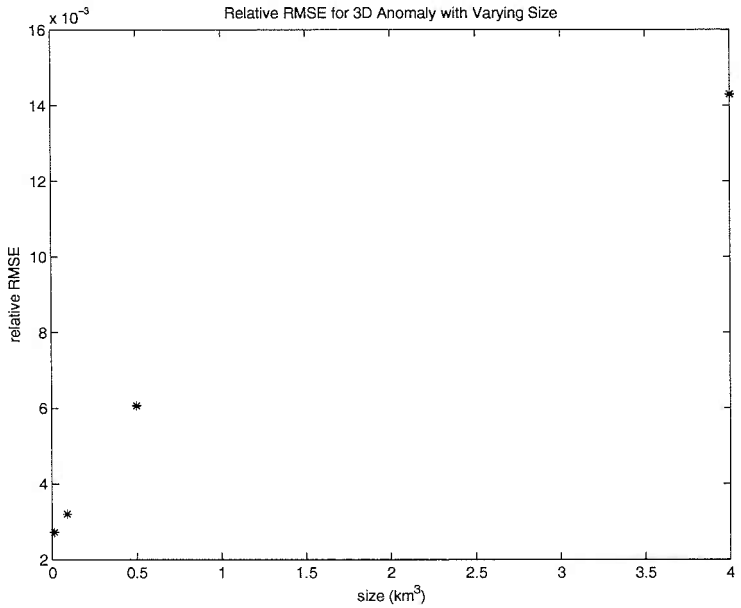

Figure 3-9: *Relative RMSEs for a* $0.303\Omega m$ *anomaly against a background of* $30\Omega m$ *with sizes of 0.0135, 0.108, 0.5 and* $4km^3$*, placed at 500 m depth and centered at the source.*

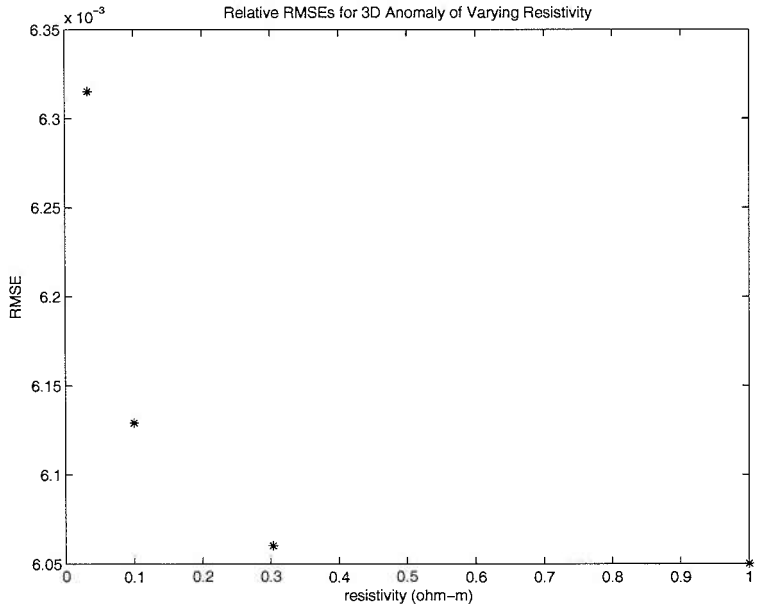

Figure 3-10: *Relative RMSEs for a 0.5* km^3*, anomaly against a background of* $30\Omega m$ *placed at 500 m depth and centered at the source, with a resistivities of 1, 0.303, 0.1 and* $0.0333\Omega m$*.*

was calculated by adding the field due to the wire, which is calculated by the 1D model. The formula was tested using 1D and 3D models which consisted of a homogeneous half-space with no topography. The results of the calculation showed the expected flat response from the 1D model, but not from the 3D model. Analysis of errors in both the anomalous and total fields suggest that this is possibly the result of errors in the total field calculation. This is because the field due to the wire is of positive sign, and is slightly larger than the negatively signed anomalous field. This results in a small positive total field. Therefore a relatively small error in the anomalous field will result in a much larger relative error when the field from the wire (which remains constant) is added to produce the total field, because the total field itself is so much smaller in magnitude.

To remove the effects of possible errors in the total field calculation I designed a method of calculating apparent resistivity using the anomalous field. This method used lookup tables to determine the apparent resistivity. The lookup tables were generated using homogeneous half-space models calculated by the 1D forward code with resistivities of 0.1 - 1Ωm increasing by 0.1Ωm increments and 1 - 100Ωm increasing by 1Ωm increments. A file was generated for each receiver recording the resistivity of the half-space and the resulting anomalous magnetic field strength. For a given model, the anomalous magnetic field generated by the `MMR3D_fwd` code is read into an array with one value of the magnetic field for each receiver. The lookup table for the receiver is then compared to the value of the magnetic field. The value in the table which is closest to that of the magnetic field is selected and the function returns the resistivity of the half-space which generated the closest value (Figure 3-11). This routine produced desired results from the 1D but not the 3D models. The fact that the 1D models gave the desired results suggests that the error lies in the calculation of the anomalous magnetic field.

To demonstrate the effects of error in the anomalous field on the apparent resistivities calculated using the above method, I added Gaussian noise to the 1D 10Ωm halfspace model, varying from 0.1 to 10%. Figure 3-12 shows the mean apparent resistivity calculated over 5,000 trials for each noise level, with error bars of one standard deviation. Some of the error bars shown here are lopsided because subtracting the standard deviation from the mean gives negative resistivity values, which are erroneous results. For this reason the error bars cut short at 0.1Ωm when the subtraction of the standard deviation yields a negative value. The figure shows that for all noise levels larger than 0.5% the apparent resistivity determined using

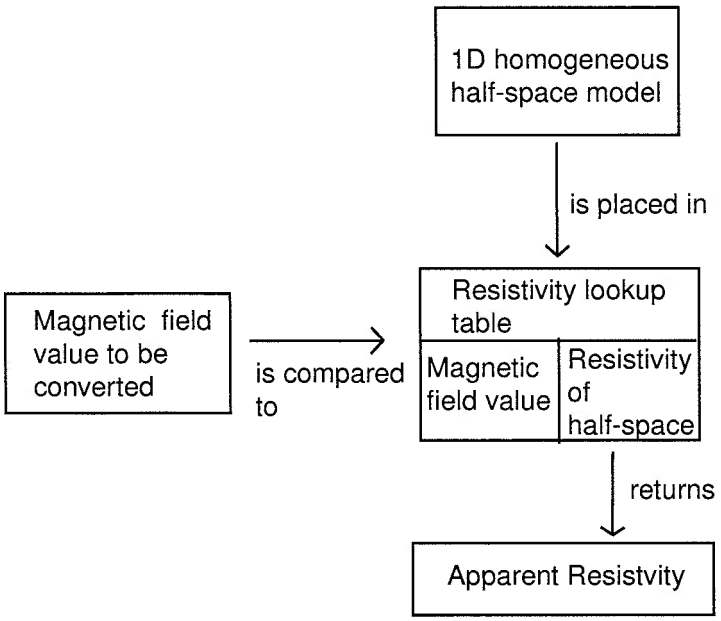

Figure 3-11: *Flowchart illustrating the function of the apparent resistivity calculation routine.*

the lookup tables can be up to 50% inaccurate within one standard deviation, (yielding 5 or $15\Omega m$ when the generating half-space is $10\Omega m$). Only 0.5% error or less generates a mean value with small enough error bars to give good results. This indicates that anomalous fields must be calculated to within 0.5% in order to produce accurate results in terms of the calculated apparent resistivity.

The desired accuracy for the anomalous magnetic field may have been achieved were it not for the memory limitation in Matlab. A larger grid may result in magnetic fields accurate enough to use the apparent resistivities. Although I am not able to use apparent resistivity as a guide, examining the magnetic fields generated by the model directly can also provide useful information about the physics of adding ridge topography to these types of MMR models.

3.3 Estimation of Data Errors

To provide a basis of comparison for the gaussian errors generated to test the apparent resistivity calculation routine in the previous section, I have estimated errors in MMR field data based on errors in not knowing the precise position of

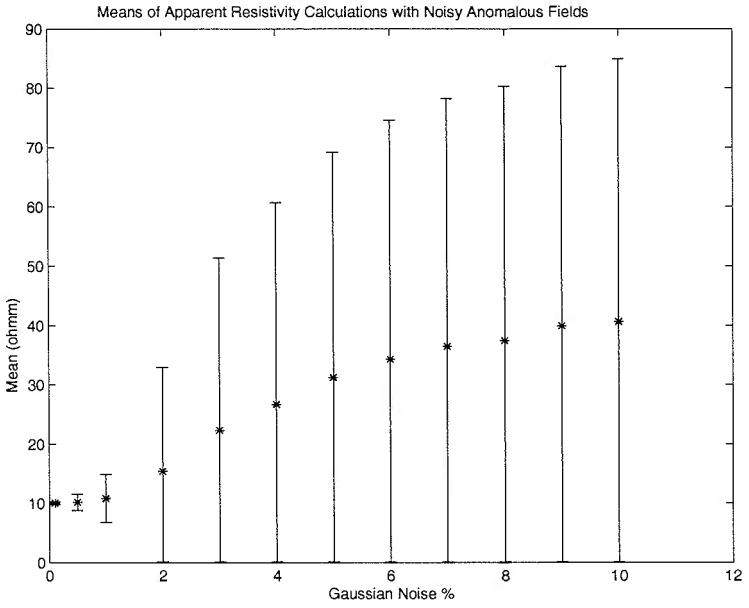

Figure 3-12: *Means of calculated apparent resistivies, from anomalous magnetic fields containing gaussian noise with levels of 0.1% to 10% of the magnetic field. The error bars plotted are one standard deviation from the mean.*

receivers and source electrodes, as these are thought to be the most significant contribution to variations in signal aside from changes in seafloor resistivity. Errors in the lateral position of the receivers can be up to 50 m, and errors in the depth of the negative source electrode can be up to 5 m.

To estimate these errors I changed the position of the 500, 1000, 2000 and 5000 m receivers by $\pm 50m$ in the 1D model of a $10\Omega m$ half-space and calculated the anomalous field. I compared these anomalous fields to one calculated for the same model with the positions of the receivers without errors. To estimate the percent error I used the following formula:

$$percenterror = \frac{|\log errorfield - \log normalfield|}{\log normalfield} * 100 \tag{3.5}$$

where **normalfield** is the anomalous field due to the model with no errors in the positions of the receivers and **errorfield** is the anomalous field due to the model with a receiver offset by 50 m. The results are summarized in figure 3-13. The highest error occurs when the first receiver is offset 50 m closer to the source at 2.12% error. The errors decrease with increasing source to receiver distance.

For models with errors in the position of the negative electrode of 5 m, the percent errors between the fields are much smaller. The mean of the errors for each receiver is 0.01%.

These results indicated that errors in the position of the receivers of 50 m yield higher noise levels than are acceptable for calculating apparent resistivities using the lookup table method. This is important to keep in mind when analyzing field data. However, errors in the position of the negative electrode yield a small enough noise level in the magnetic field to generate accurate apparent resistivities.

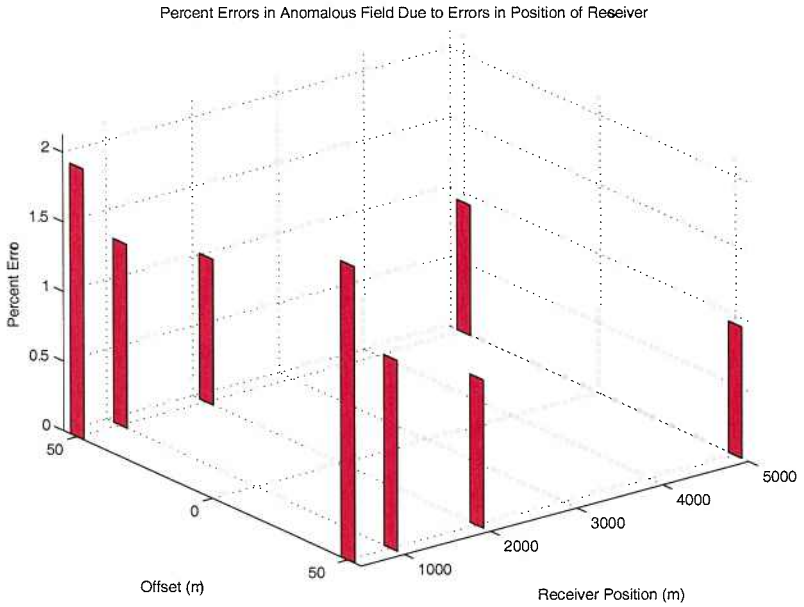

Figure 3-13: *Percent errors in the anomalous magnetic field due to errors in the position of the receivers.*

Chapter 4

Ridge Topography Models

Adding ridge topography to MMR models proved to be an arduous task. For each ridge model the mesh in the z-direction needed to be altered to provide the correct cell dimensions to represent the topography. The heights of the ridge for each cell needed to be input individually. Because topography is relatively difficult to put into these models, I decided to only use models of ridges that are geometrically simple. All of the modeled ridges have constant heights in the y-direction. Ridge heights in the x-direction approximate a constant slope and are symmetric about $x = 0$. The resistivity beneath the seafloor is uniform. Because the magnetic field has an integrative nature and is not affected by small scale heterogeneities, I feel that these simplistic ridge geometries nevertheless provide a useful insight into the behavior of the seafloor magnetic field in an MMR experiment.

To study the effects of various geometrical factors on the impact of the ridge on the MMR data, I varied several properties of the ridge: slope, resistivity, the placement of receivers and the placement of the source (figures 4-1 - 4-4). The range of slopes was designed to include and go beyond realistic slopes of flanks of the EPR. Estimating from bathymetric profiles yielded examples of slopes of 0.05 to 0.2 [Scheirer and MacDonald, 1993]. The slopes investigated were 0.05, 0.0667, 0.2, and 0.4, corresponding to rises of 150, 200, 600, and 1200 m over a distance of 3000 m. The resistivity of the ridges were determined based on the range of resistivities of the oceanic crust up to 1 km depth reported by [Evans, 1994]. The resistivities used were 1, 3, 10, 30 and 100 Ωm. Each resistivity/slope combination was run with 4 different combinations of source and receiver placement abbreviated as configs 1, 2, 3 and 4 (Figures 4-1 - 4-4). Configs 1 and 2 have the source placed on the ridge

axis and configs 3 and 4 have the source off the ridge axis. Configs 1 and 3 have receivers along the slope of the ridge, and configs 2 and 4 have receivers along the ridge axis. Note that the source when placed off-axis is placed on the opposite side of the ridge from the receivers.

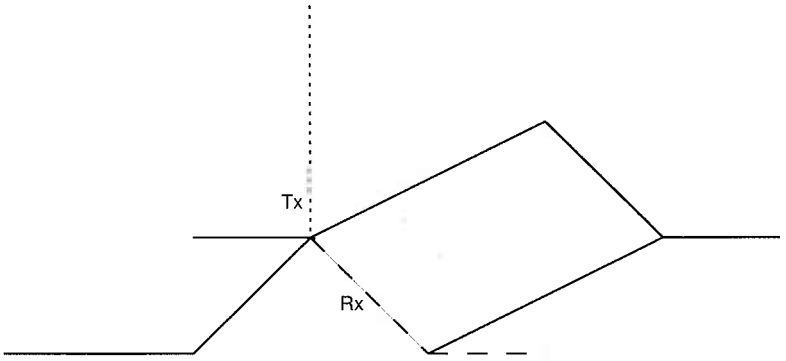

Figure 4-1: *Config 1 - receivers are placed along the ridge slope and the transmitter is located on the ridge axis*

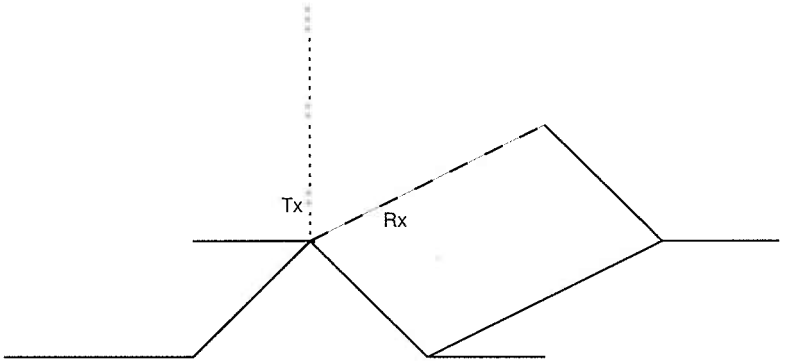

Figure 4-2: *Config 2 - receivers are placed along the ridge axis and the transmitter is located on the ridge axis*

To provide a baseline for comparison, homogeneous half-space models are run with the same mesh as the topography models for each slope, resistivity and source position combination. The relative RMSEs are also calculated for each model. The relative RMSE is defined as:

$$relRMSE = \sqrt{\frac{1}{n}\sum_{i=1}^{n}\left(\frac{ridge(i)}{hhs(i)} - 1\right)^2} \tag{4.1}$$

where **n** is the number of receivers, **ridge** is the magnetic field due to the ridge, and **hhs** is the magnetic field due to a flat, homogeneous half-space. The same mesh is

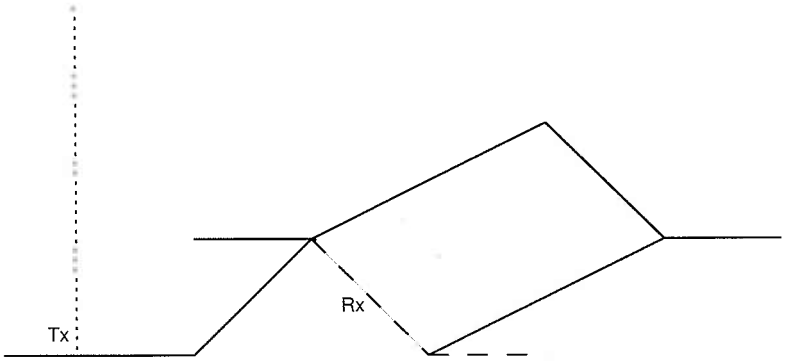

Figure 4-3: *Config 3 - receivers are placed along the ridge slope and the transmitter is located off the ridge axis*

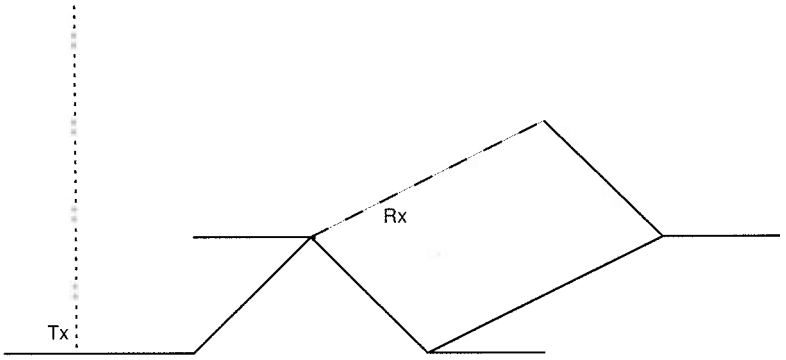

Figure 4-4: *Config 4 - receivers are placed along the ridge axis and the transmitter is located off the ridge axis*

used for both flat and ridge topography models in order to try to subtract the effects of the mesh such as errors near the source due to small mesh sizes. The magnetic fields corresponding with these models are also analyzed to determine the ridge's impact.

The RMSE and relative RMSEs are used as metrics of the contribution of the ridge topography to the magnetic fields. High RMSEs and relative RMSEs result from models where the calculated anomalous magnetic field is very different from the field generated by flat topography. Thus the higher the RMSEs and the relative RMSEs, the more the ridge topography is contributing to the anomalous magnetic field.

Based on the physics behind the MMR technique one can make some simple assumptions about the expected behavior of the RMSEs. In the presence of ridge topography the approximation of a flat seafloor is invalid or configurations with the source on the ridge axis (configs 1 and 2) new current paths through the seawater

are created. In this case the slope of the ridge causes seawater to replace much of the volume between the source and the receivers which would be under the seafloor in a flat topography (figure 4-5). Therefore more current travels through a less resistive medium (seawater) resulting in, we predict, a less negative anomalous field, and therefore a larger total magnetic field.

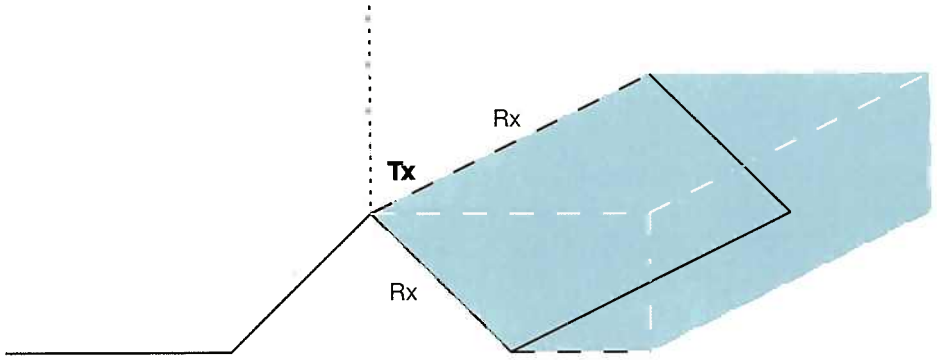

Figure 4-5: *Configs 1 and 2, receivers are placed along the ridge axis and the ridge slope. The transmitter is located on the ridge axis, the blue volume represents the volume of subsurface replaced seawater compared to a flat topography*

For configurations with the source off the ridge axis (configs 3 and 4) current paths through the seawater are closed. The resistive ridge intercedes between the source and the receivers (figure 4-6, distorting the current flow patterns and, we predict, resulting in a smaller total magnetic field (more negative anomalous field.)

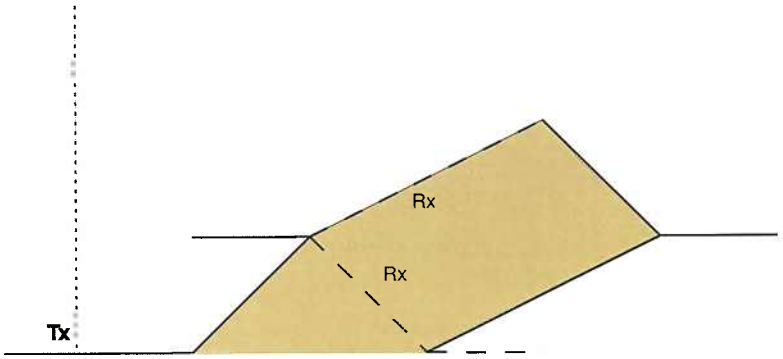

Figure 4-6: *Configs 3 and 4, receivers are placed along the ridge axis and the ridge slope. The transmitter is located off the ridge axis, the brown volume represents the volume of seawater replaced by the ridge compared to a flat topography*

The results from the models bear out these assumptions. The behavior of the relative RMSEs are shown below (Figures 4-7 - 4-10). Plotting the RMSEs shows a difference between the behavior of the relative RMSEs versus the absolute RMSEs.

For slopes of 0.2 and 0.4 the change in RMSE was different between ridges of 1 and $3\Omega m$, than the change in relative RMSE. Review of the magnetic fields, shows that this difference comes from noise in the response of the first and second receivers. The relative RMSE appears to me to be a more robust metric of the effect of ridge topography on the magnetic fields, and so I am using it rather than the regular RMSE as a basis for my conclusions.

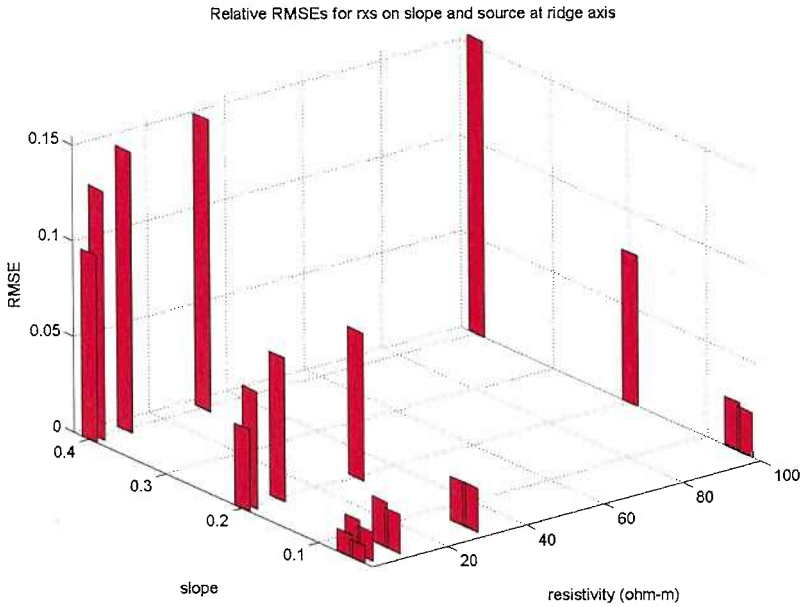

Figure 4-7: *Config 1 - Relative RMSEs for ridges with varying slopes and resistivites. The source is on the ridge axis, and the receivers are on the slope of the ridge.*

Examining the magnetic fields from models using a 1 ohm-m resistivity half-space and slopes of 0.05, 0.0667, 0.2, 0.4, demonstrates the effect of current traveling through conductive seawater to reach receivers. The distance plotted on the x-axis in the following figures is the 3D distance from the top of the ridge axis in the x-z plane y=0 to the receiver. In figure 4-11 (config 1) the steeper the slope of the ridge, the less negative the anomalous magnetic field, resulting in a larger total field and a decrease in the apparent resistivity. The addition of ridge topography restructures the material below the transmitter. When the transmitter is on top of the ridge on the ridge axis, the volume beneath the transmitter includes both seawater and the half-space bounded by the seafloor (figure 4-5). The additional seawater (conductive) component allows more of the current to pass through the volume and therefore generates a less negative magnetic field strength with increasing slope. As the distance from the source increases the magnetic fields for

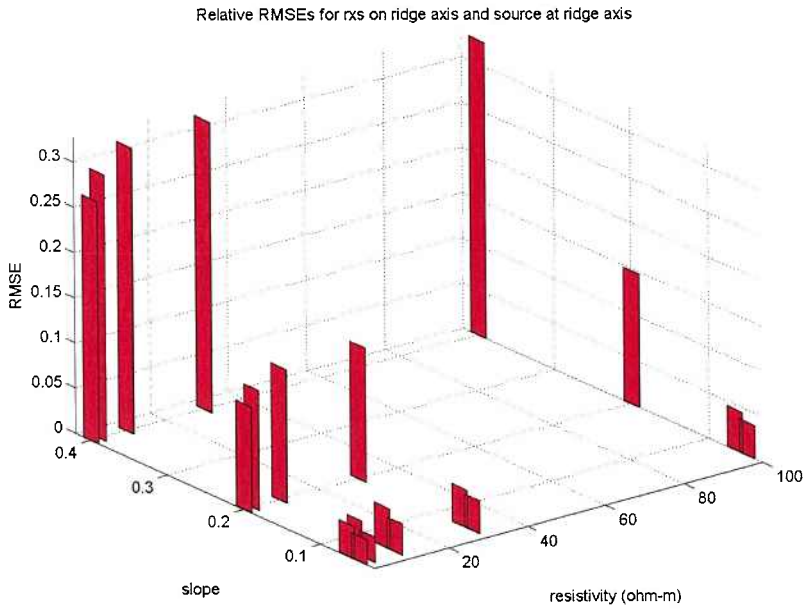

Figure 4-8: *Config 2 - Relative RMSEs for ridges with varying slopes and resistivites. The source is on the ridge axis, and the receivers are also on the axis of the ridge.*

different slopes become indistinguishable. At larger source to receiver distances the current has to travel through more of the resistive subsurface and decreases the effects of the topography. The effects of the topography are, however, significant at all source to receiver distances for this configuration

Figure 4-12 (config 2) shows the magnetic fields from the same models with both the source and receivers on the ridge axis. The magnetic fields quickly become almost indistinguishable as the distance from the source increases. Because the source and the receivers are placed on the ridge axis the current reaching the receivers has traveled a path parallel to and beneath the ridge axis. This means that the added seawater volume beneath the source does not contribute much to the magnetic fields. In this case source to receiver distances greater than 2500m show no significant effects from the topography.

Figures 4-13 and 4-14 (configs 3 and 4) show the magnetic fields from the same models with the source off the ridge at 3000 m later distance from the ridge axis, and receivers along the ridge slope, and along the ridge axis respectively. The behavior of the magnetic fields with increasing slope is very different from the models with the source at the ridge axis. For these models the anomalous magnetic fields are more negative with increasing slope. This results in a lower total magnetic

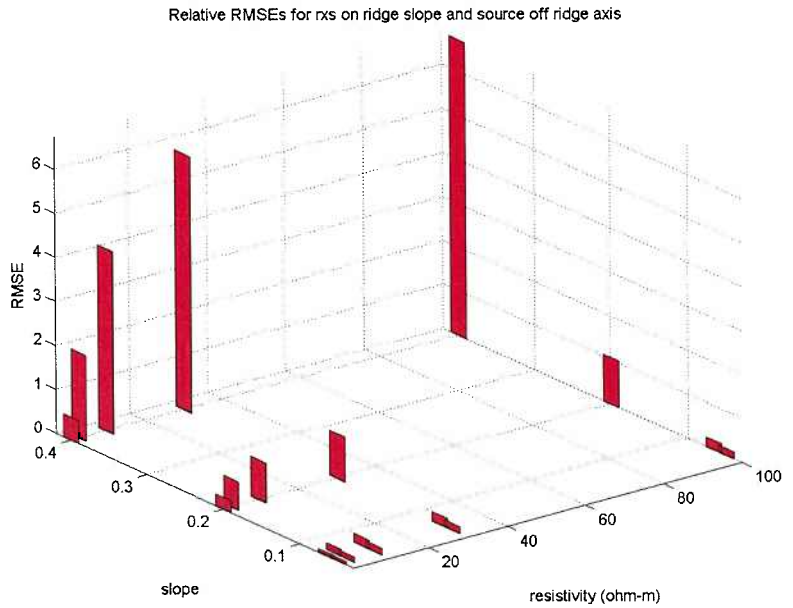

Figure 4-9: *Config 3 - Relative RMSEs for ridges with varying slopes and resistivites. The source is off the ridge axis, and the receivers are on the slope of the ridge.*

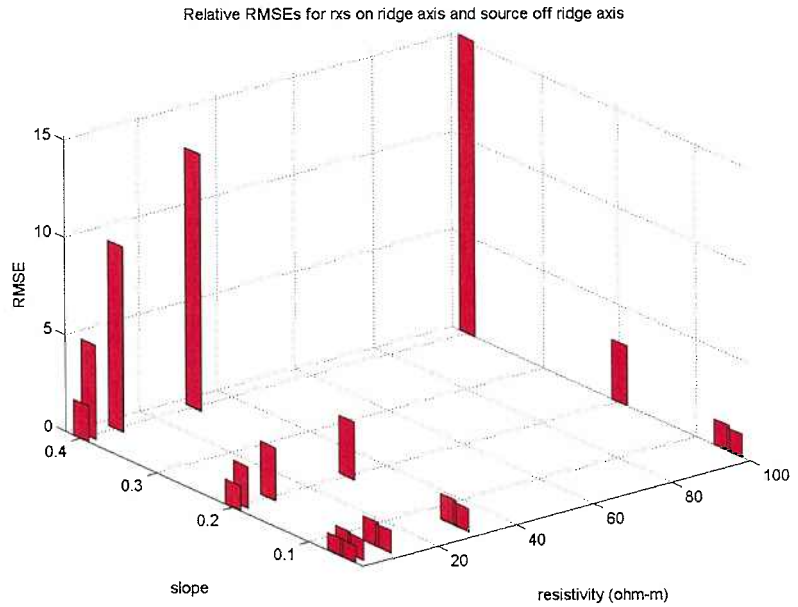

Figure 4-10: *Config 4 - Relative RMSEs for ridges with varying slopes and resistivites. The source is off the ridge axis, and the receivers are on the axis of the ridge.*

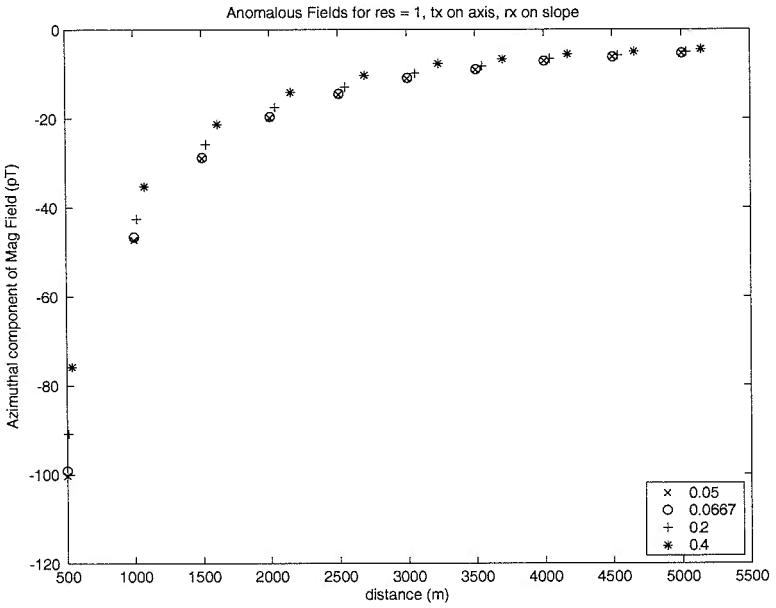

Figure 4-11: *Config 1 - Magnetic fields for ridges with seafloor resistivities of 1 ohm-m. The current source is placed on the ridge axis, while the receivers are along the slope and each symbol represents a different slope as shown in the legend.*

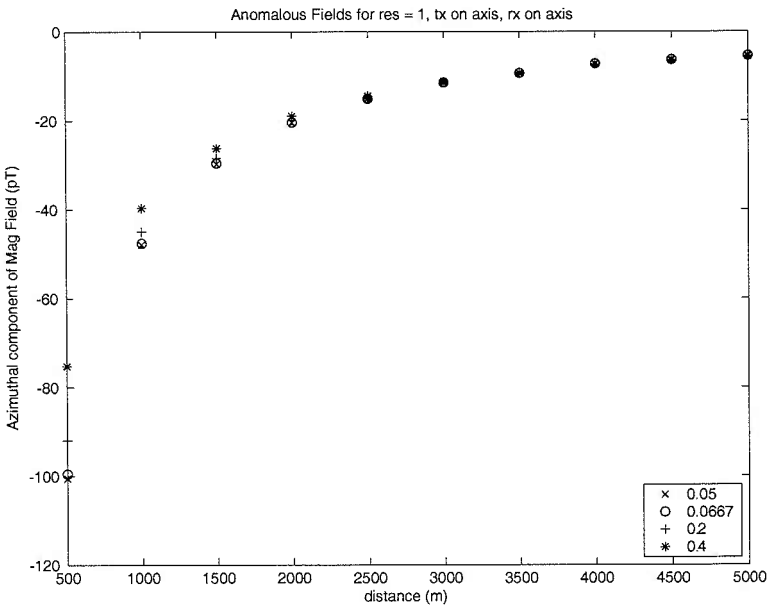

Figure 4-12: *Config 2 - Magnetic fields for ridges with seafloor resistivities of 1 ohm-m. The current source is placed on the ridge axis, while the receivers are along the axis and each symbol represents a different slope as shown in the legend.*

field and a higher apparent resistivity. This is because the volume beneath the transmitter is solely the resistive half-space and for receivers on the ridge, the current has to travel through more of the half-space, allowing less current to reach the receivers (figure 4-6). The steeper the slope the larger the volume of resistive half-space that the current has to travel through to reach the receivers.

Figure 4-13 shows a change in the shape of the magnetic fields beyond a distance of approximately 6000 m. The distance plotted is the distance from the source on the other side of the ridge, these changes occur where the receivers are on the flat and no longer on the ridge. The receivers placed beyond 6000 m show a different contribution from the ridge as they are no longer plotted on the ridge slope but are beyond the ridge. Because this behavior of the magnetic fields is consistent for all resistivities tested, the remainder of these plots are shown in appendix A.

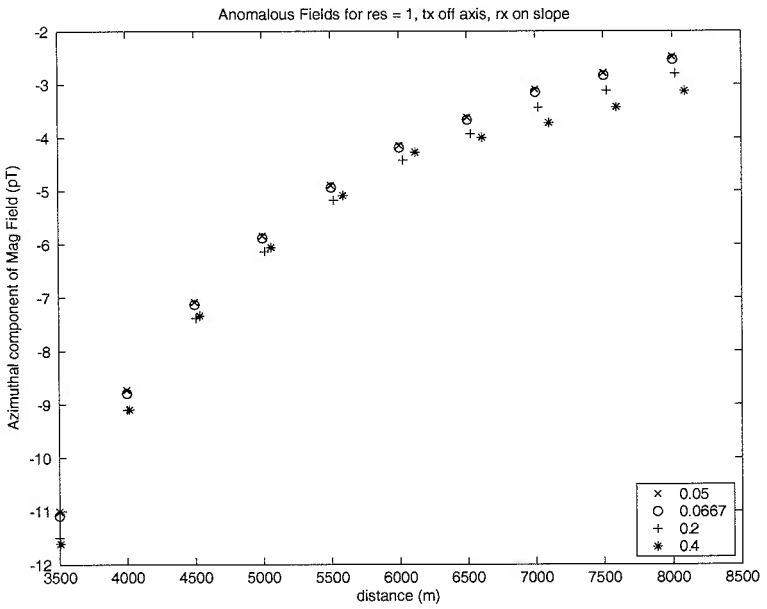

Figure 4-13: *Config 3 - Magnetic fields for ridges with seafloor resistivities of 1 ohm-m. The current source is placed off the ridge axis, while the receivers are along the slope and each symbol represents a different slope as shown in the legend.*

It is also useful to look at the response of the magnetic fields to a change in resistivity. To do this the magnetic fields are plotted for a given slope and varying resistivity. Consistent throughout all source/receiver placement geometries, the magnetic field becomes more negative with increasing resistivity. This is because the more resistive the volume beneath the source the less current can reach the receiver which will cause a smaller magnetic field (figs 4-15 - 4-18).

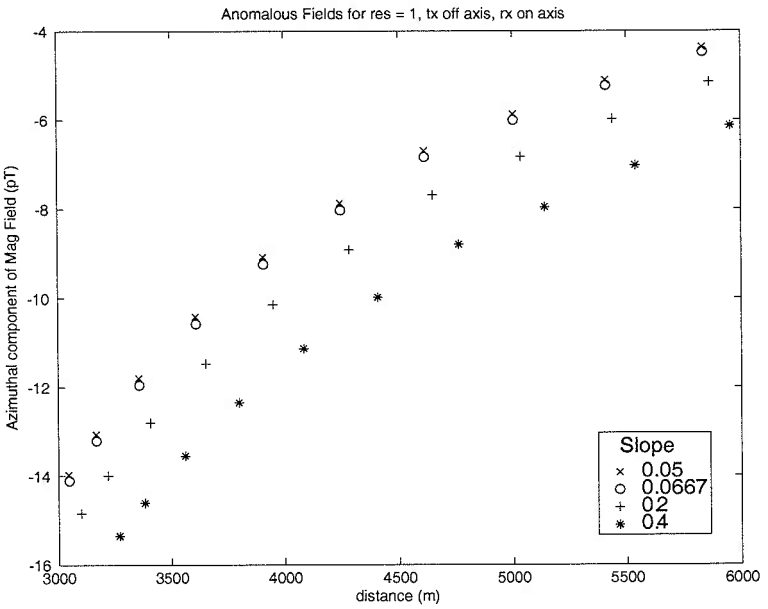

Figure 4-14: *Config 4 - Magnetic fields for ridges with seafloor resistivities of 1 ohm-m. The current source is placed off the ridge axis, while the receivers are along the ridge and each symbol represents a different slope as shown in the legend.*

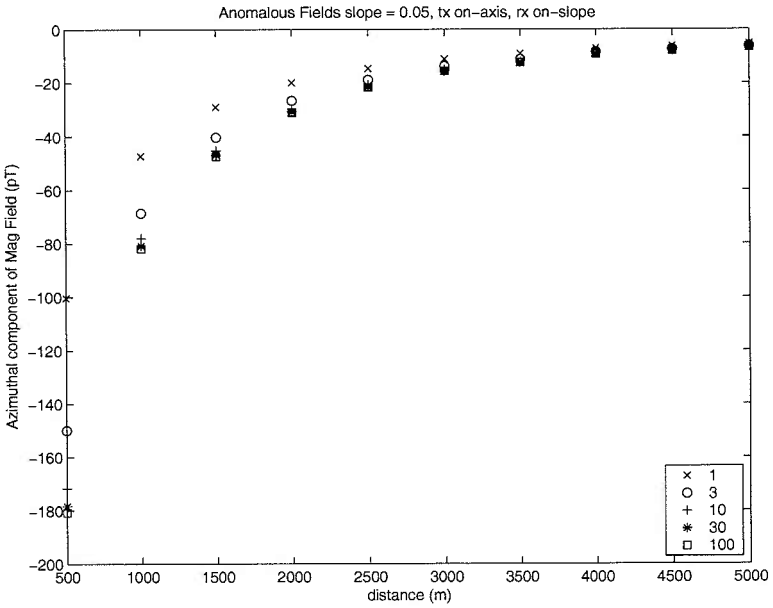

Figure 4-15: *Config 1 - Magnetic fields for ridges with slopes of 0.05. The current source is placed on the ridge axis, while the receivers are along the slope and each symbol represents a different resistivity as shown in the legend.*

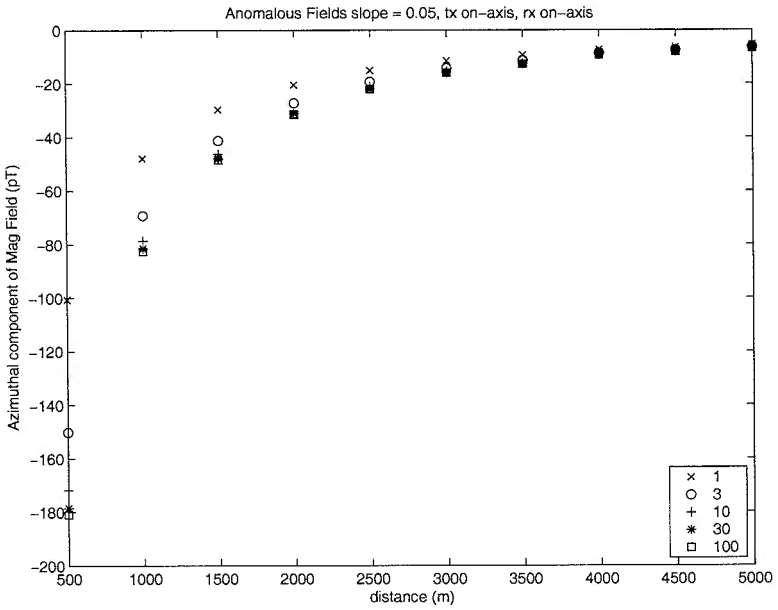

Figure 4-16: *Config 2 - Magnetic fields for ridges with slopes of 0.05. The current source is placed on the ridge axis, while the receivers are along the axis and each symbol represents a different resistivity as shown in the legend.*

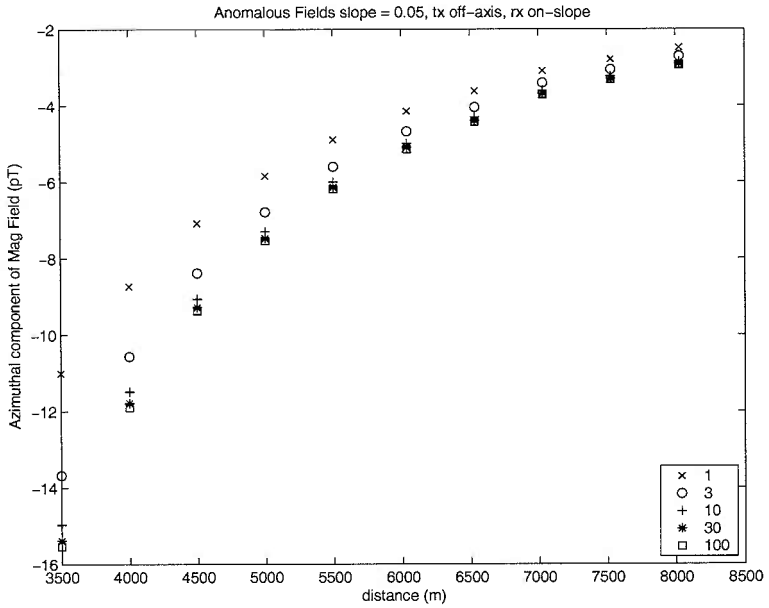

Figure 4-17: *Config 3 - Magnetic fields for ridges with slopes of 0.05. The current source is placed off the ridge axis, while the receivers are along the slope and each symbol represents a different resistivity as shown in the legend.*

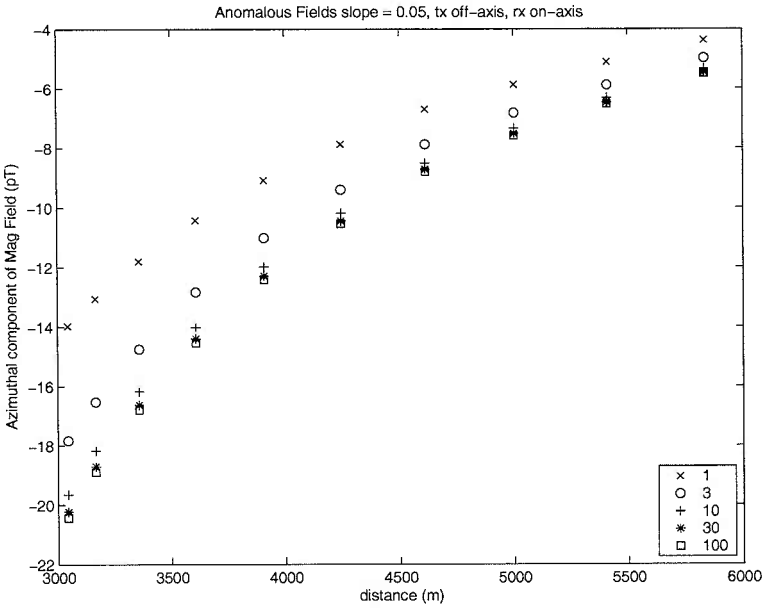

Figure 4-18: *Config 4 - Magnetic fields for ridges with a slope of 0.05. source is off-axis, receivers are along ridge axis and each symbol represents a different resistivity as shown in the legend.*

The placement of the source and receivers is also a control on the size of the magnetic fields. In all cases the anomalous magnetic field amplitudes are smaller for the models which had the source off of the ridge axis. The anomalous magnetic field amplitudes are lower because with the source off the ridge axis the current paths from the source to receivers are longer and travel through more of the resistive subsurface. Because these plots show similar behavior for all slopes the remainder are found in the appendix B.

Results for ridges with config 1				
Filename	Resistivity	Slope	RMSE	Relative RMSE
rt12x	1	0.05	0.987205	0.027415
rt17x	3	0.05	1.876553	0.027962
rt4x	10	0.05	2.36756	0.034345
rt13x	30	0.05	2.52761	0.036208
rt11x	100	0.05	2.589686	0.03678
rt2x	1	0.0667	1.213446	0.035719
rt18x	3	0.0667	2.330832	0.039323
rt1x	10	0.0667	2.973789	0.044554
rt14x	30	0.0667	3.178106	0.041441
rt3x	100	0.0667	3.271886	0.045149
rt6x	1	0.2	4.168854	0.116602
rt19x	3	0.2	7.741496	0.132571
rt5x	10	0.2	9.756006	0.147424
rt15x	30	0.2	10.42491	0.147965
rt7x	100	0.2	10.671634	0.147503
rt9x	1	0.4	8.434251	0.267879
rt20x	3	0.4	15.101824	0.294317
rt8x	10	0.4	18.948627	0.316114
rt16x	30	0.4	20.243386	0.321181
rt10x	100	0.4	20.784268	0.327162

Results for ridges with config 2				
Filename	Resistivity	Slope	RMSE	Relative RMSE
rt12y	1	0.05	0.725074	0.008906
rt17y	3	0.05	1.610264	0.014983
rt4y	10	0.05	2.105313	0.020447
rt13y	30	0.05	2.272567	0.022981
rt11y	100	0.05	2.335415	0.023577
rt2y	1	0.0667	0.836001	0.011548
rt18y	3	0.0667	1.827135	0.018194
rt1y	10	0.0667	2.373774	0.023691
rt14y	30	0.0667	2.54293	0.022854
rt3y	100	0.0667	2.618913	0.025631
rt6y	1	0.2	3.10802	0.042677
rt19y	3	0.2	6.221476	0.061328
rt5y	10	0.2	7.868733	0.075115
rt15y	30	0.2	8.400701	0.076928
rt7y	100	0.2	8.595599	0.078397
rt9y	1	0.4	7.065957	0.097692
rt20y	3	0.4	12.675052	0.129879
rt8y	10	0.4	15.442619	0.146717
rt16y	30	0.4	16.324553	0.152254
rt10y	100	0.4	16.647758	0.154501

Results for ridges with config 3				
Filename	Resistivity	Slope	RMSE	Relative RMSE
r012x	1	0.05	0.461891	0.067612
r017x	3	0.05	0.846881	0.121555
r04x	10	0.05	1.047624	0.14761
r013x	30	0.05	1.113556	0.155727
r011x	100	0.05	1.137712	0.158601
r02x	1	0.0667	0.524327	0.078673
r018x	3	0.0667	1.091891	0.161944
r01x	10	0.0667	1.351866	0.198919
r014x	30	0.0667	1.439664	0.211195
r03x	100	0.0667	1.472131	0.215707
r06x	1	0.2	1.62206	0.270135
r019x	3	0.2	3.138882	0.644596
r05x	10	0.2	3.950091	0.910452
r015x	30	0.2	4.228988	1.019021
r07x	100	0.2	4.32547	1.057771
r09x	1	0.4	2.565485	0.524164
r020x	3	0.4	5.304041	1.956801
r08x	10	0.4	6.891512	4.151674
r016x	30	0.4	7.458292	5.831246
r010x	100	0.4	7.666393	6.730022

Results for ridges with config 4				
Filename	Resistivity	Slope	RMSE	Relative RMSE
r012y	1	0.05	3.969134	0.860446
r017y	3	0.05	5.460499	1.062089
r04y	10	0.05	6.171435	1.142655
r013y	30	0.05	6.398881	1.166127
r011y	100	0.05	6.481243	1.174329
r02y	1	0.0667	4.040334	0.883571
r018y	3	0.0667	5.799758	1.157451
r01y	10	0.0667	6.584895	1.267342
r014y	30	0.0667	6.839326	1.301305
r03y	100	0.0667	6.93209	1.313484
r06y	1	0.2	5.59232	1.261303
r019y	3	0.2	8.308837	2.131355
r05y	10	0.2	9.693689	2.733127
r015y	30	0.2	10.1592	2.976739
r07y	100	0.2	10.321268	3.063926
r09y	1	0.4	7.19592	1.834207
r020y	3	0.4	11.171434	4.832694
r08y	10	0.4	13.357337	9.521365
r016y	30	0.4	14.121002	13.204071
r010y	100	0.4	14.401299	15.195008

Chapter 5

Conclusions and Future Work

5.1 Conclusions

Verification of the 3D modeling code carried out in chapter 3 shows that the 3D models are sensitive to resistive layers and conductive anomalies in the subsurface. The change in the magnetic fields are controlled by the resistivity of the structure and its placement in the subsurface. The change in the apparent resistivity can be predicted using the change in the anomalous magnetic field as a guide, a more negative anomalous field yields a larger apparent resistivity. The impact of the ridge structure for each configuration is presented in the table below.

Rules of thumb for Apparent Resistivities		
Configuration	Increase Slope	Increase Resistivity
1	Decreased (but small)	Increased
2	Decreased (but small)	Increased
3	Increased	Increased
4	Increased	Increased

Attempts to use apparent resistivities to gauge the impact of ridge topography were unsuccessful. Apparent resistivity is very sensitive to noise, and thus noise levels greater than 0.5% of the field yield inaccurate apparent resistivities. The magnetic fields generated by `MMR3d_fwd` of homogeneous half-spaces do not yield accurate apparent resistivities. Because of this apparent resistivities were not used to analyze the results.

The impact of ridge topography on MMR models is controlled by the slope of the

ridge, the resistivity of the subsurface, and the geometry of the source and receiver locations. While all of the ridge topographies modeled caused a change in the magnetic field from that of a homogeneous half-space, those with large slopes had the largest impact. Based on this observation, a good rule of thumb would be that ridges with slopes of 0.2 and larger should definitely be modeled using ridge topography and not a flat seasurface. For ridges with slopes as low as 0.05 and 0.0667, topography can most likely be neglected if small amounts of error are acceptable. The EPR at 9°50'N has a slope of approximately 0.05, and therefore ridge topography may be neglected in inversion of the data from Evans et al. [2000].

Geometries with the receivers along the ridge axis (configs 1 and 3) have a higher error when compared to a flat topography than those with receivers along the ridge (configs 2 and 4). For a geometry with the source on the ridge axis and the receivers along the slope of the ridge (config 1), the impact of the slope of the ridge on the magnetic field decreases as the source to receiver distance increases. This is also true for geometries with the source on the axis and the receivers along the ridge axis (config 2). In this case the magnetic fields are almost indistinguishable at source to receiver distances of 3000 m.

In the case of the source being placed off the ridge axis a very different behavior is observed. If the receivers are placed on the slope of the ridge (config 3), the magnetic fields are very similar until the receivers are beyond the ridge, at which point the differences between magnetic fields of ridges with different slopes becomes more pronounced. In the case of the receivers being placed on the ridge axis (config 4) the differences of the fields are consistent for all source to receiver spacings.

These differences suggest that whether or not ridge topography needs to be included in forward modeling and inversion routines is largely based on the geometry of the source and receiver locations. It would be too simplistic to suggest a single rule of thumb for whether to include ridge topography in MMR models, for this reason I present one for each of the source/receiver geometries.

1) For ridges with the source on the axis and receivers along the slope of the ridge (config 1), ridge topography should be included in modeling if the source to receiver distances are smaller than 3 km (this distance threshold is based on the specific models I have run. The relative RMSEs for this configuration are small compared to those for configurations 3 and 4.

2) Likewise for ridges with the source on the axis and receivers on the axis of the

ridge (config 2). The relative RMSEs for this configuration are small compared to those for configurations 3 and 4.

3) For ridges with the source off the ridge axis and receivers along the slope (config 3), inclusion of the ridge topography is important if receivers extend beyond the ridge on the other side.

4) For ridges with the source off the ridge axis and receivers on the ridge axis (config 4) topography should be included regardless of source to receiver distances.

5.2 Future Work

This work was hindered by three restrictions: 1) the difficulty of adding topography to the models, 2) the limitations imposed on mesh size by Matlab, and 3) the inaccuracy of the calculation of the anomalous magnetic fields which is linked to restriction 2 . The next logical step for this type of modeling is to examine the effects of more realistic topography on MMR data. Models with more realistic topography are very difficult to generate using `MMR3d_fwd` because the code lacks a GUI interface. Although MMR is integrative and insensitive to small scale inhomogeneities, `MMR3d_fwd` requires a symmetric geometry which is not entirely realistic for Mid Ocean Ridges. The simplicity of the topographies usable in these models make it difficult to mimic the topography of real ridges, which is important for analysis of MMR data for studies of ridges like the EPR [Evans et al., 2002].

The memory restriction of 2 GB in Matlab also created an insurmountable barrier. This memory restriction is not code dependent, and is a result of the Matlab development environment. It is likely with a larger mesh size the errors in the calculated magnetic fields would not have been large enough to prevent analysis using apparent resistivities. If similar modeling is done using a code without these restrictions, then the analysis of the apparent resistivities could provide an understanding of the effects of ridge topography on inversion of MMR data for studies like the one referenced above.

This work showed that in some cases ridge topography produces a non-negligible effect on MMR data and provided some simple guidelines for when ridge topography ought to be included in MMR models, however, more work needs to be done to adequately understand the effects of more realistic topography in order to analyze

the results of MMR studies on Mid Ocean Ridges.

Appendix A

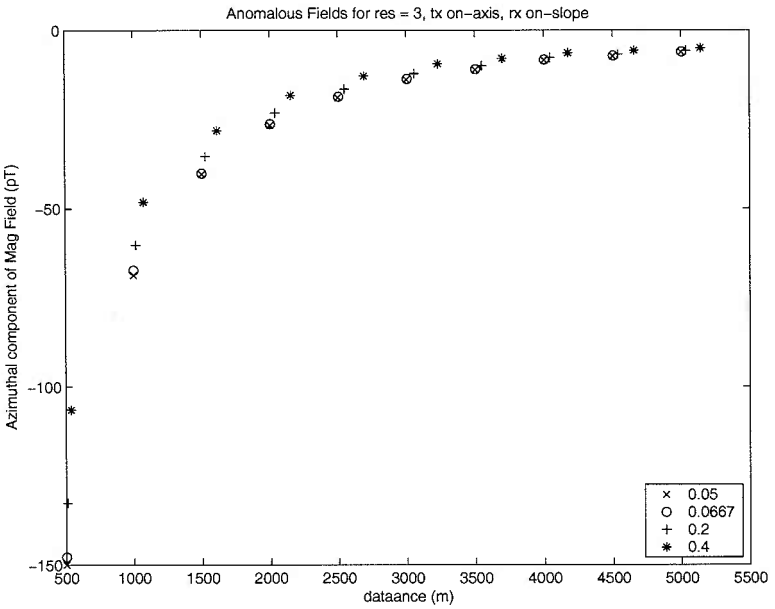

Figure A-1: *Config 1 - Magnetic fields for ridges with seafloor resistivities of 3 ohm-m. The current source is placed on the ridge axis, while the receivers are along the slope and each symbol represents a different slope as shown in the legend.*

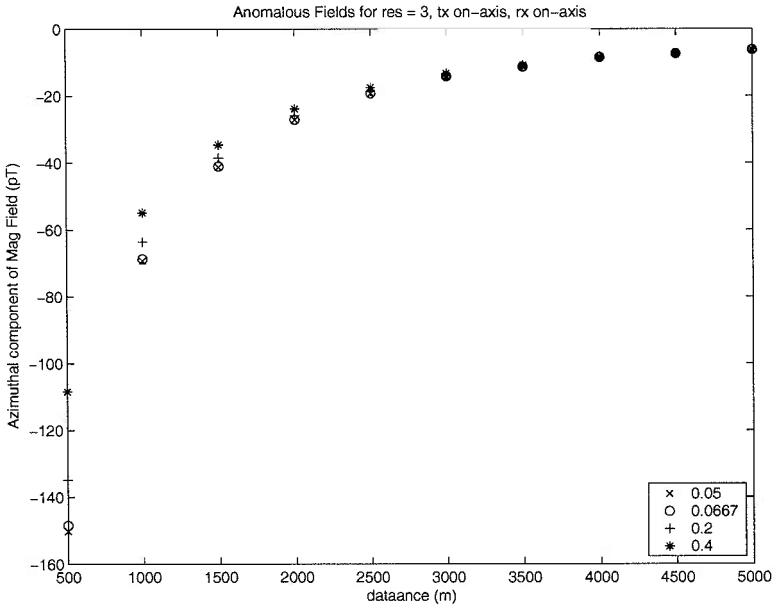

Figure A-2: *Config 2 - Magnetic fields for ridges with seafloor resistivities of 3 ohm-m. The current source is placed on the ridge axis, while the receivers are along the axis and each symbol represents a different slope as shown in the legend.*

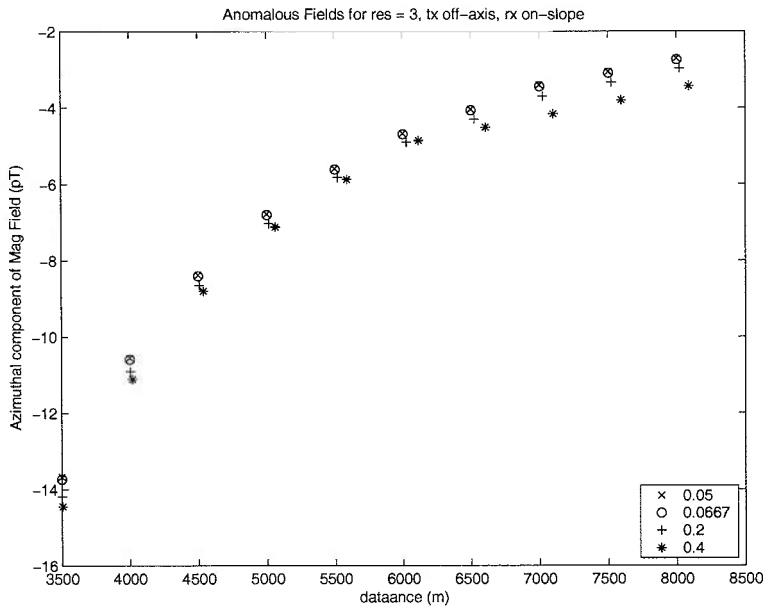

Figure A-3: *Config 3 - Magnetic fields for ridges with seafloor resistivities of 3 ohm-m. The current source is placed off the ridge axis, while the receivers are along the slope and each symbol represents a different slope as shown in the legend.*

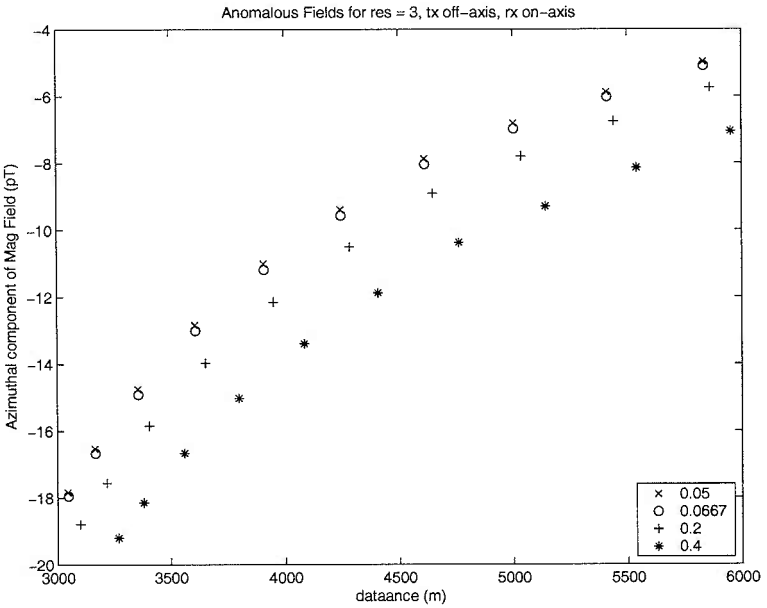

Figure A-4: *Config 4 - Magnetic fields for ridges with seafloor resistivities of 3 ohm-m. The current source is placed off the ridge axis, while the receivers are along the axis and each symbol represents a different slope as shown in the legend.*

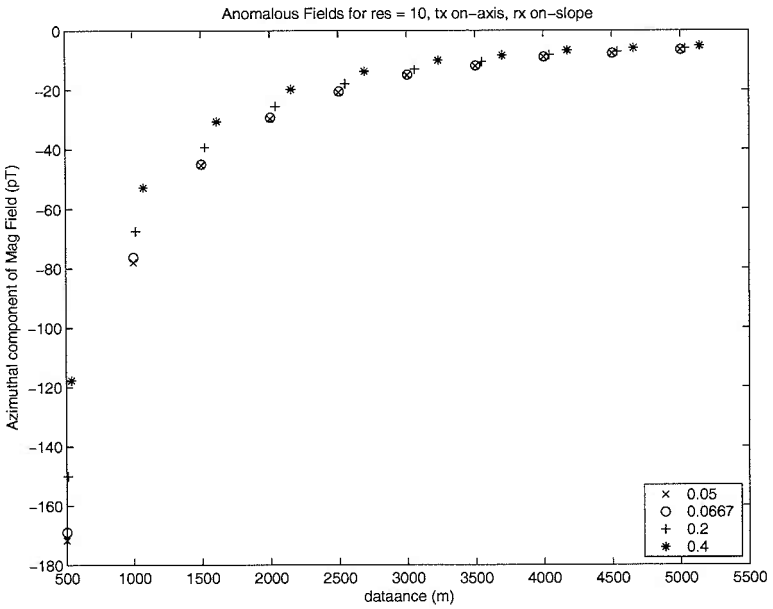

Figure A-5: *Config 1 - Magnetic fields for ridges with seafloor resistivities of 10 ohm-m. The current source is placed on the ridge axis, while the receivers are along the slope and each symbol represents a different slope as shown in the legend.*

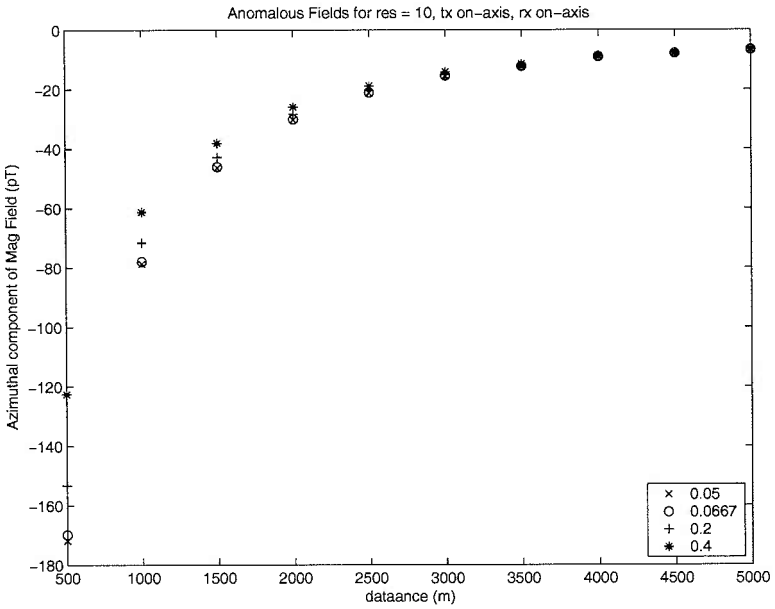

Figure A-6: *Config 2 - Magnetic fields for ridges with seafloor resistivities of 10 ohm-m. The current source is placed on the ridge axis, while the receivers are along the axis and each symbol represents a different slope as shown in the legend.*

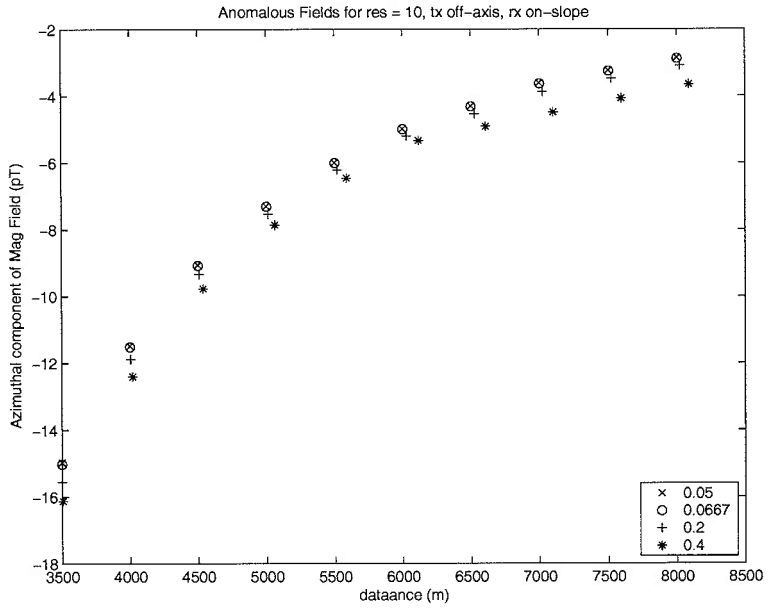

Figure A-7: *Config 3 - Magnetic fields for ridges with seafloor resistivities of 10 ohm-m. The current source is placed off the ridge axis, while the receivers are along the slope and each symbol represents a different slope as shown in the legend.*

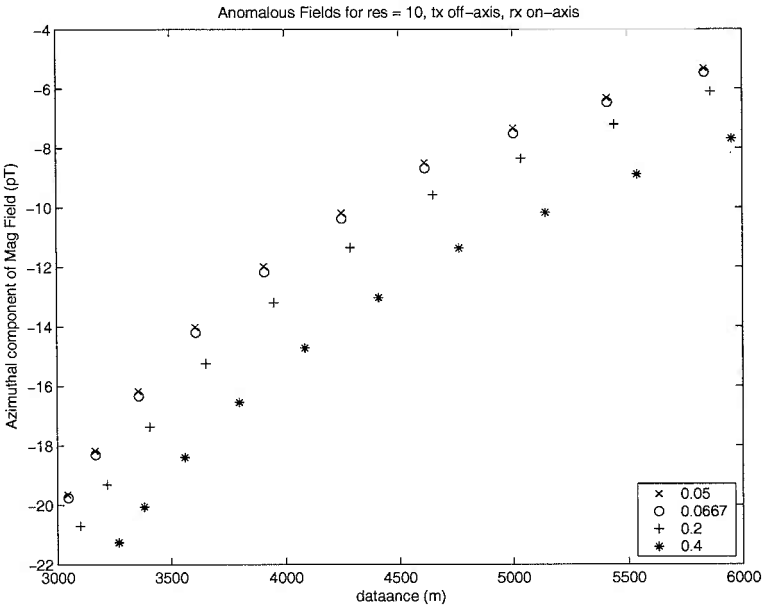

Figure A-8: *Config 4 - Magnetic fields for ridges with seafloor resistivities of 10 ohm-m. The current source is placed off the ridge axis, while the receivers are along the axis and each symbol represents a different slope as shown in the legend.*

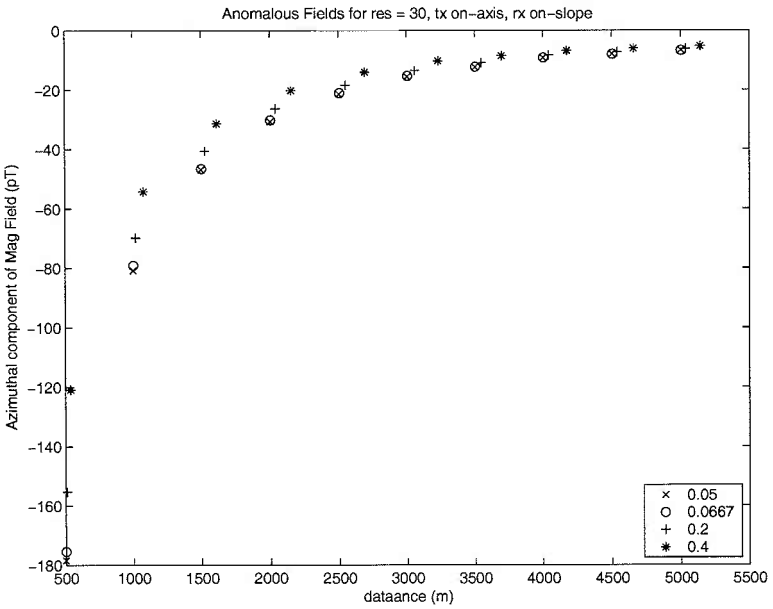

Figure A-9: *Config 1 - Magnetic fields for ridges with seafloor resistivities of 30 ohm-m. The current source is placed on the ridge axis, while the receivers are along the slope and each symbol represents a different slope as shown in the legend.*

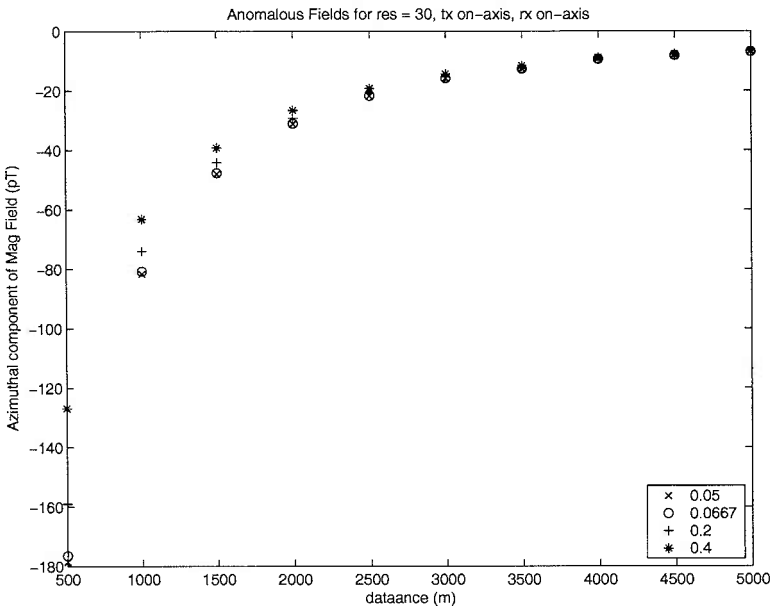

Figure A-10: *Config 2 - Magnetic fields for ridges with seafloor resistivities of 30 ohm-m. The current source is placed on the ridge axis, while the receivers are along the axis and each symbol represents a different slope as shown in the legend.*

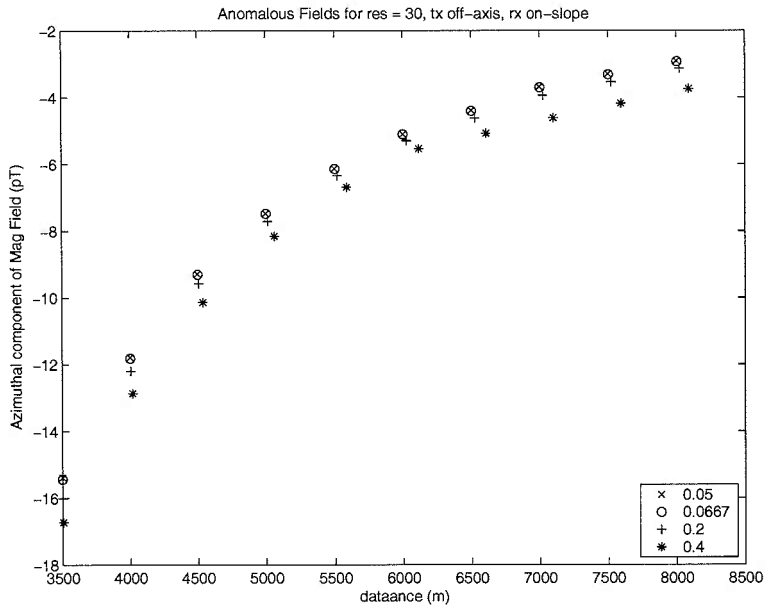

Figure A-11: *Config 3 - Magnetic fields for ridges with seafloor resistivities of 30 ohm-m. The current source is placed off the ridge axis, while the receivers are along the slope and each symbol represents a different slope as shown in the legend.*

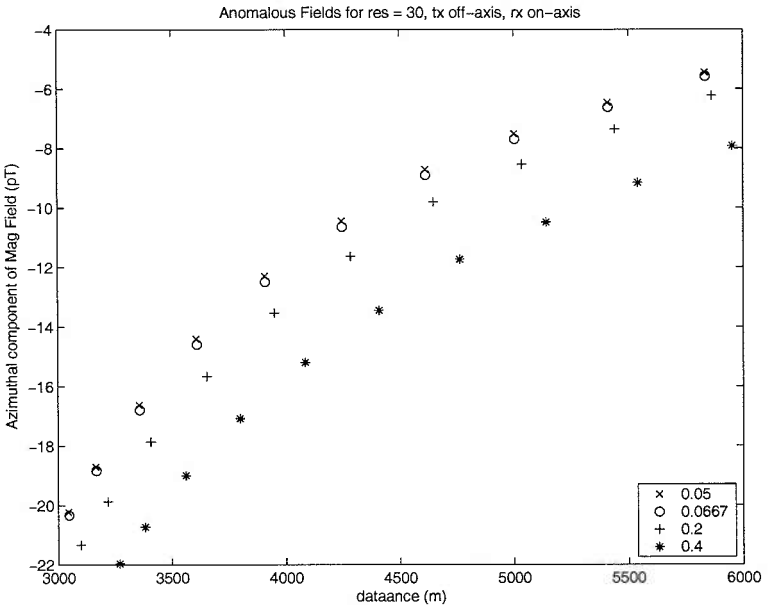

Figure A-12: *Config 4 - Magnetic fields for ridges with seafloor resistivities of 30 ohm-m. The current source is placed off the ridge axis, while the receivers are along the axis and each symbol represents a different slope as shown in the legend.*

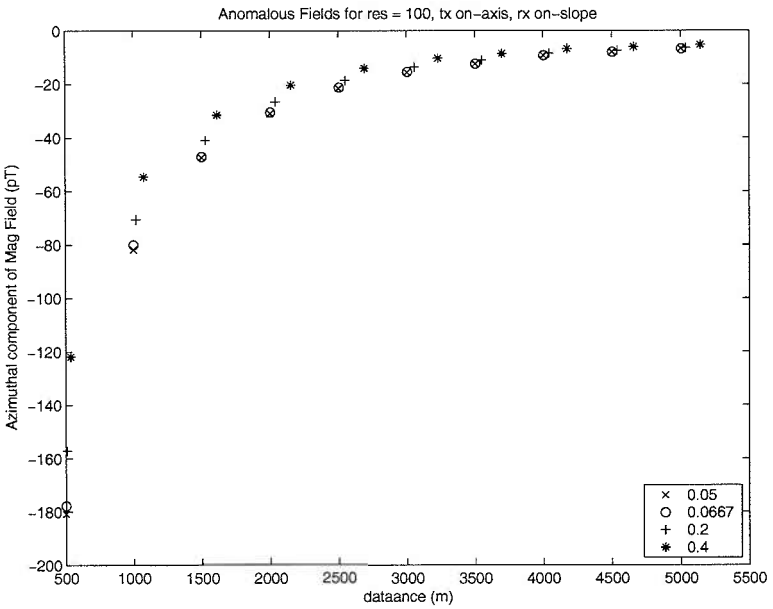

Figure A-13: *Config 1 - Magnetic fields for ridges with seafloor resistivities of 100 ohm-m. The current source is placed on the ridge axis, while the receivers are along the slope and each symbol represents a different slope as shown in the legend.*

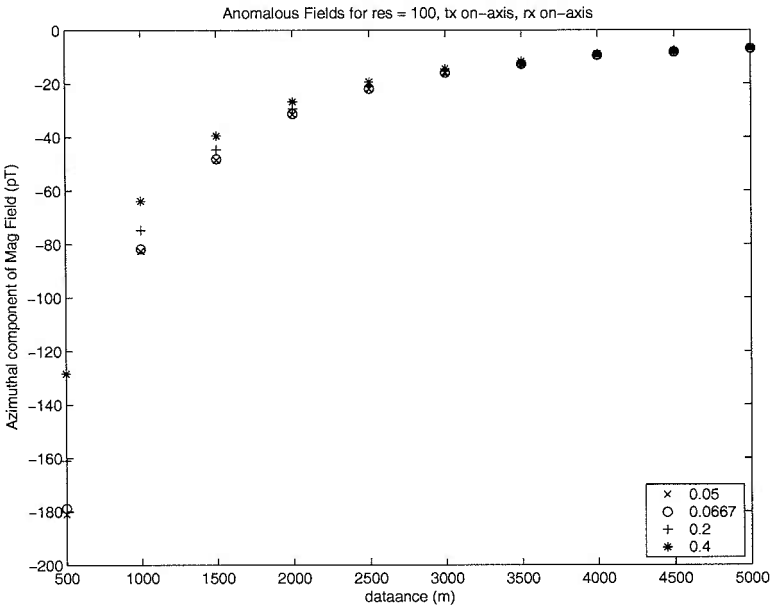

Figure A-14: *Config 2 - Magnetic fields for ridges with seafloor resistivities of 100 ohm-m. The current source is placed on the ridge axis, while the receivers are along the axis and each symbol represents a different slope as shown in the legend.*

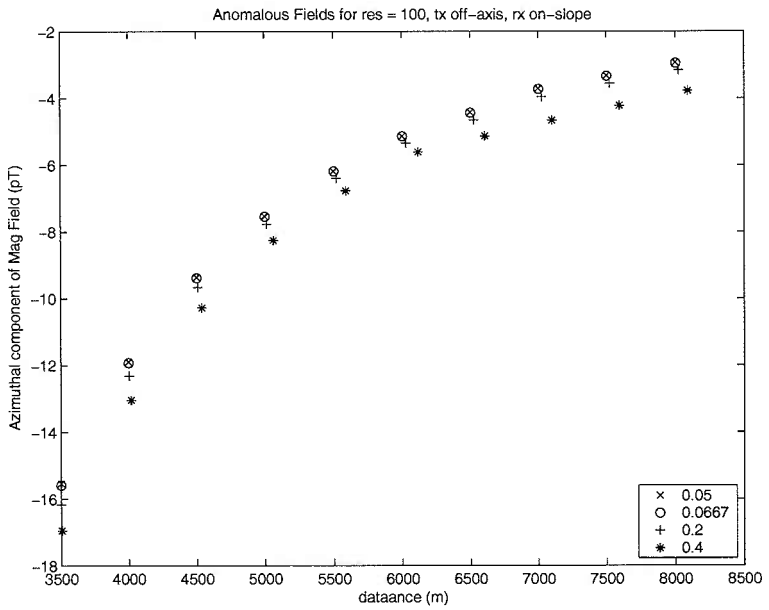

Figure A-15: *Config 3 - Magnetic fields for ridges with seafloor resistivities of 100 ohm-m. The current source is placed off the ridge axis, while the receivers are along the slope and each symbol represents a different slope as shown in the legend.*

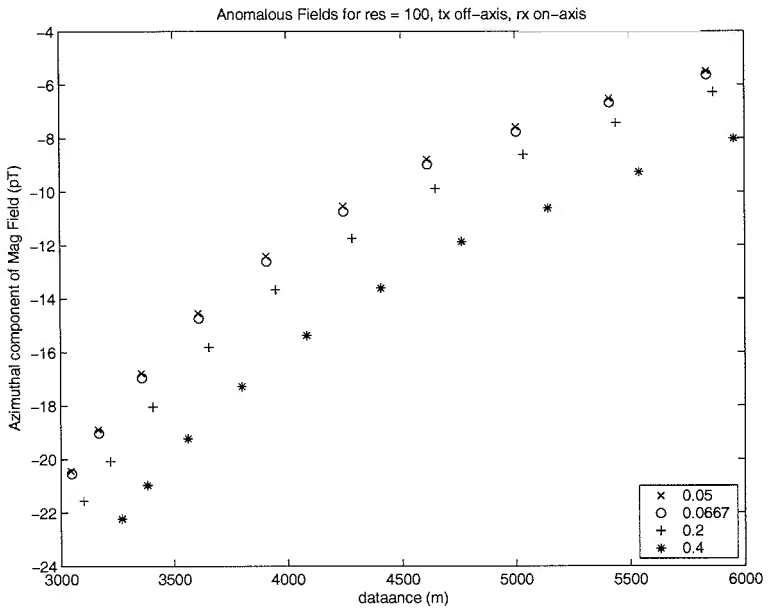

Figure A-16: *Config 4 - Magnetic fields for ridges with seafloor resistivities of 100 ohm-m. The current source is placed off the ridge axis, while the receivers are along the axis and each symbol represents a different slope as shown in the legend.*

Appendix B

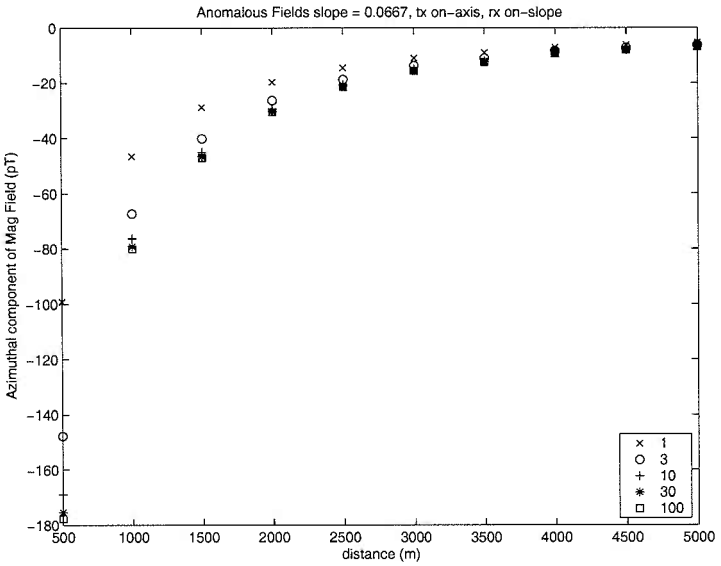

Figure B-1: *Config 1 - Magnetic fields for ridges with slopes of 0.0667. The current source is placed on the ridge axis, while the receivers are along the slope and each symbol represents a different resistivity as shown in the legend.*

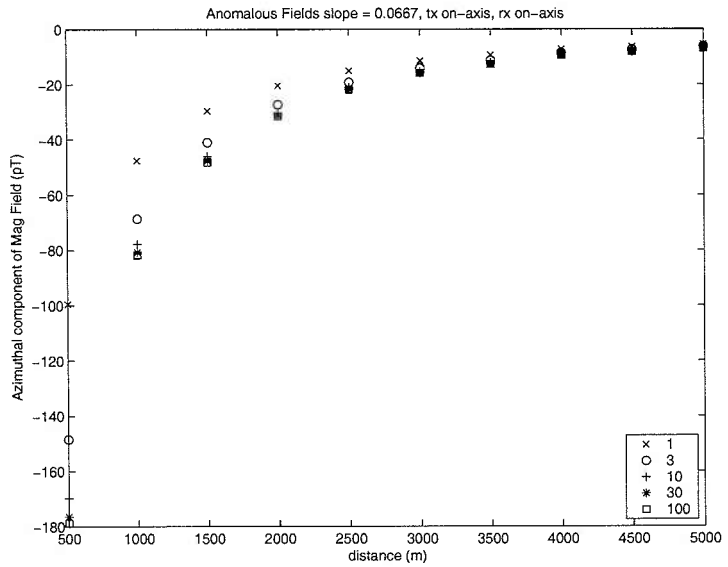

Figure B-2: *Config 2 - Magnetic fields for ridges with slopes of 0.0667. The current source is placed on the ridge axis, while the receivers are along the axis and each symbol represents a different resistivity as shown in the legend.*

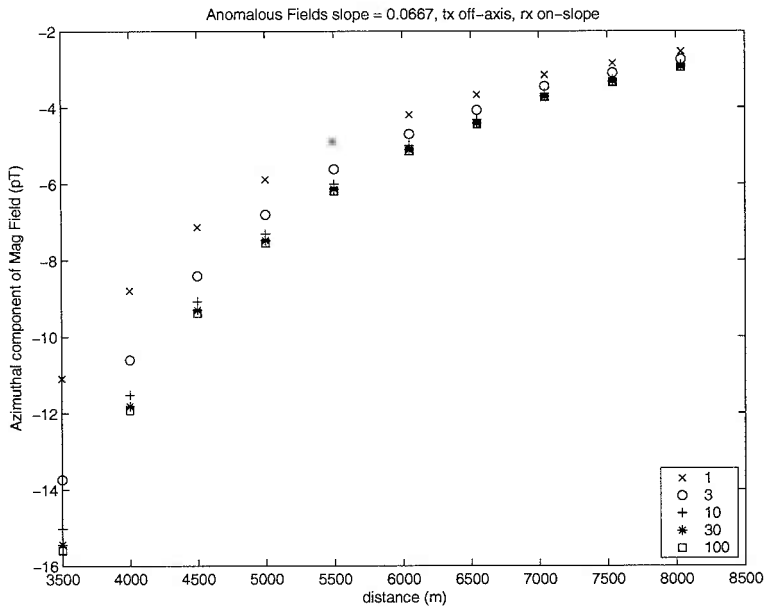

Figure B-3: *Config 3 - Magnetic fields for ridges with slopes of 0.0667. The current source is placed off the ridge axis, while the receivers are along the slope and each symbol represents a different resistivity as shown in the legend.*

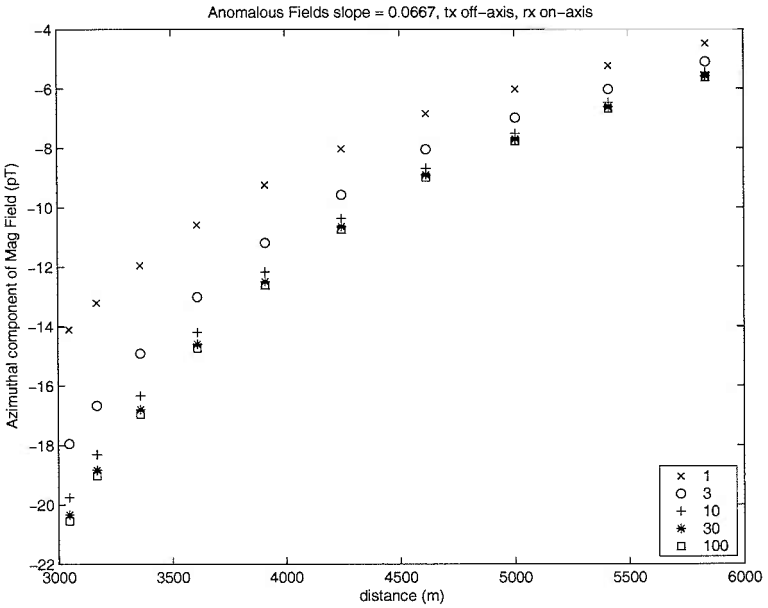

Figure B-4: *Config 4 - Magnetic fields for ridges with slopes of 0.0667. The current source is placed off the ridge axis, while the receivers are along the axis and each symbol represents a different resistivity as shown in the legend.*

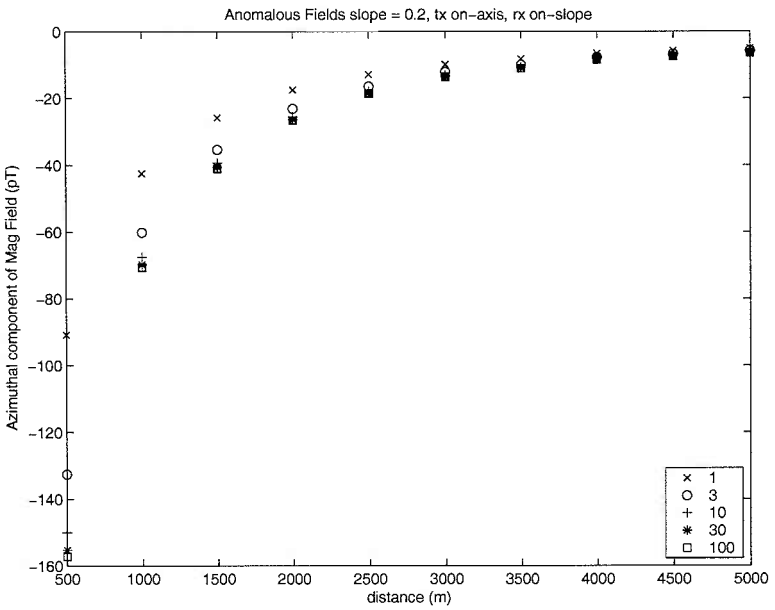

Figure B-5: *Config 1 - Magnetic fields for ridges with slopes of 0.2. The current source is placed on the ridge axis, while the receivers are along the slope and each symbol represents a different resistivity as shown in the legend.*

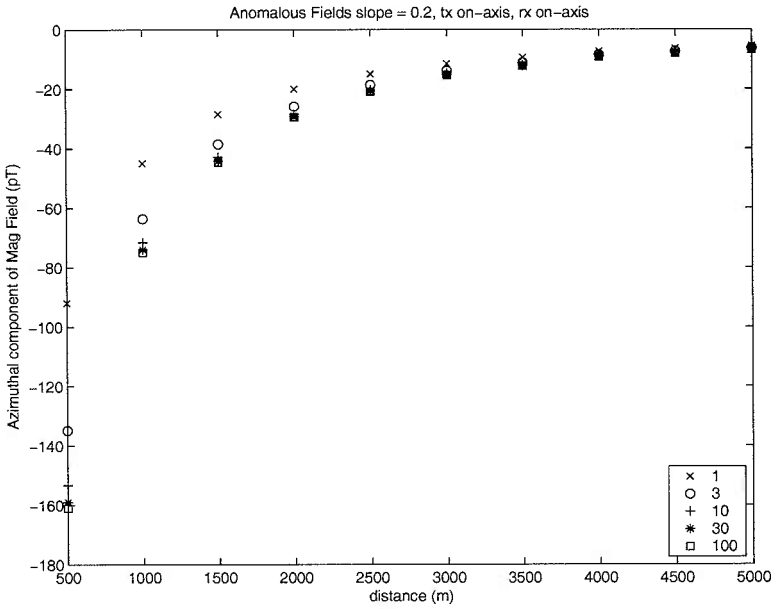

Figure B-6: *Config 2 - Magnetic fields for ridges with slopes of 0.2. The current source is placed on the ridge axis, while the receivers are along the axis and each symbol represents a different resistivity as shown in the legend.*

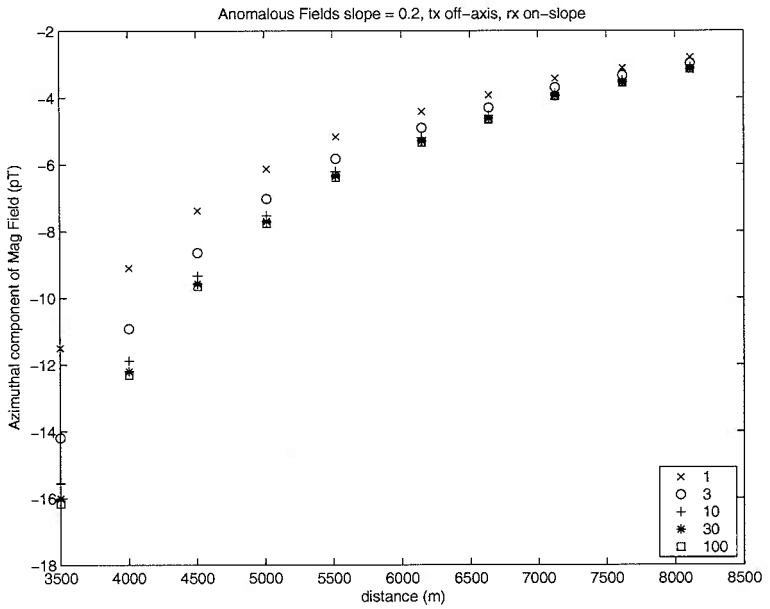

Figure B-7: *Config 3 - Magnetic fields for ridges with slopes of 0.2. The current source is placed off the ridge axis, while the receivers are along the slope and each symbol represents a different resistivity as shown in the legend.*

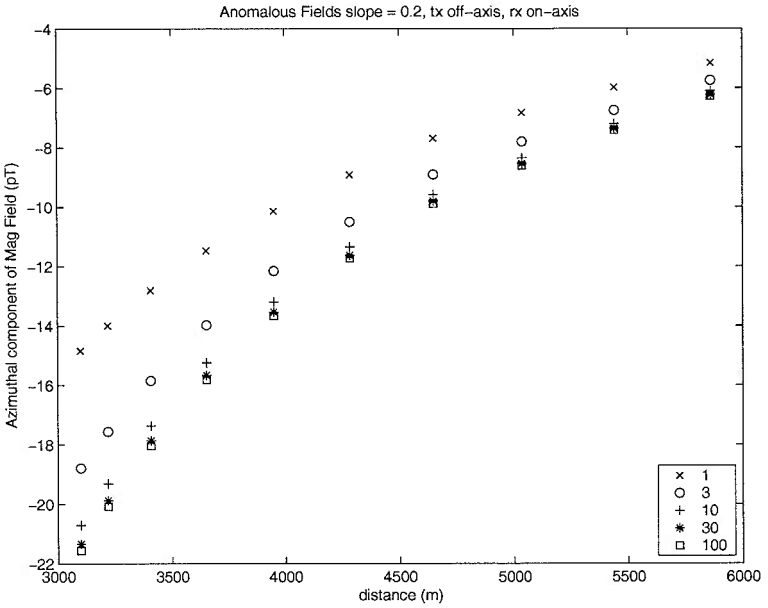

Figure B-8: *Config 4 - Magnetic fields for ridges with slopes of 0.2. The current source is placed off the ridge axis, while the receivers are along the axis and each symbol represents a different resistivity as shown in the legend.*

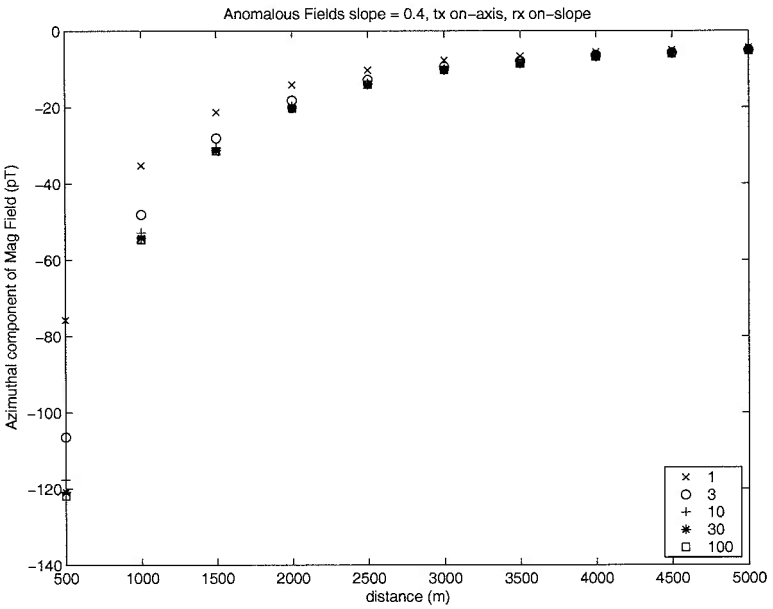

Figure B-9: *Config 1 - Magnetic fields for ridges with slopes of 0.4. The current source is placed on the ridge axis, while the receivers are along the slope and each symbol represents a different resistivity as shown in the legend.*

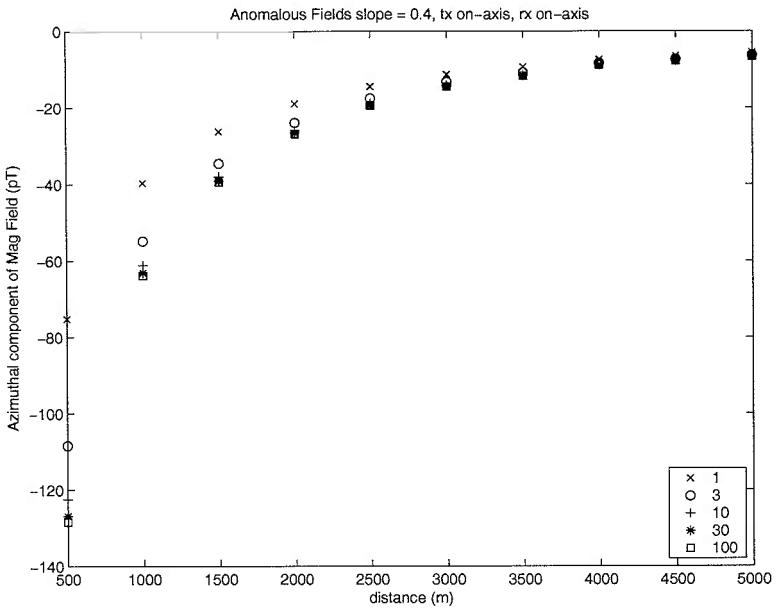

Figure B-10: *Config 2 - Magnetic fields for ridges with slopes of 0.4. The current source is placed on the ridge axis, while the receivers are along the axis and each symbol represents a different resistivity as shown in the legend.*

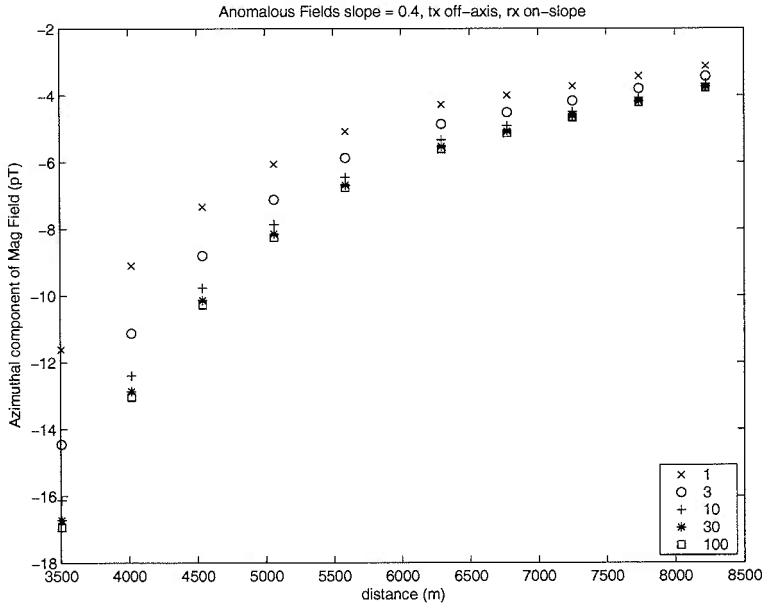

Figure B-11: *Config 3 - Magnetic fields for ridges with slopes of 0.4. The current source is placed off the ridge axis, while the receivers are along the slope and each symbol represents a different resistivity as shown in the legend.*

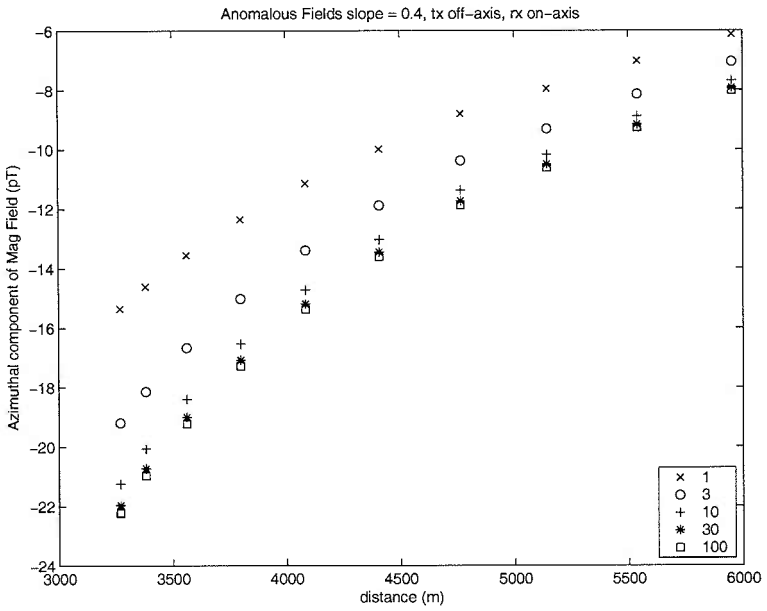

Figure B-12: *Config 4 - Magnetic fields for ridges with slopes of 0.4. The current source is placed off the ridge axis, while the receivers are along the axis and each symbol represents a different resistivity as shown in the legend.*

Bibliography

[Archie, 1942] Archie, G. (1942). The electrical resistivity log as an aid in determining some reservoir characteristics. *J. Petrol. Technol.*, 8:1–8.

[Chave et al., 1991] Chave, A., Constable, S., and Edwards, R. (1991). Electrical exploration methods for the seafloor. *Electromagnetic Methods in Applied Geophysics: Investigations in Geophysics: Soc. Expl. Geophys. edited by Nabighan, M.N.*, pages 931–986.

[Chen et al., 2002] Chen, J., Haber, E., and Oldenburg, D. (2002). Three-dimensional numerical modeling and inversion of magnetmetric resistivity data. *Geophys. J. Int.*, 149:679–697.

[Detrick et al., 1987] Detrick, R., Buhl, P., Vera, E., Mutter, J., Orcutt, J., Madsen, J., and Brocher, T. (1987). Multi-channel seismic imaging of a crustal magma chamber along the east pacific rise. *Nature*, 326:33–41.

[Edwards, 1974] Edwards, R. (1974). The magnetometric resistivity method and its application to the mapping of a fault. *Can. J. Earth Sci.*, 11:1136–1156.

[Edwards et al., 1981] Edwards, R., Law, L., and DeLaurier, J. (1981). On measuring the electrical conductivity of the oceanic crust by a modified magnetometric resistivity method. *J. of Geophys. Res.*, 86(B12):11609–11615.

[Edwards et al., 1984] Edwards, R., Nobes, D., and Gomez-Trevino, E. (1984). Offshore electrical exploration of sedimentary basins: The effects of anisotropy in horizontally isotropic, layered media. *Geophysics*, 49(5):566–576.

[Evans, 1994] Evans, R. (1994). Constraints on the large-scale porosity and permeability structure of young oceanic crust from velocity and resistivity data. *Geophys. J. Int.*, 119:869–879.

[Evans et al., 1998] Evans, R., Webb, S., Jegen, M., and Sananikone, K. (1998). Hydrothermal circulation at the cleft-vance overlapping spreading center: results of a magnetometric resistivity survey. *J. of Geophys. Res.*, 103(B6):12321–12338.

[Evans et al., 2002] Evans, R., Webb, S., and Team, R.-U. (2002). Crustal resistivity structure at 9°50' n on the east pacific rise: results of an electromagnetic survey. *Geophys. R. Letters*, 29(6):1.

[Scheirer and MacDonald, 1993] Scheirer, D. and MacDonald, K. (1993). Variation in cross-sectional area of the axial ridge along the east pacific rise; evidence for the magmatic budget of a fast spreading center. *Journal of Geophysical Research, B, Solid Earth and Planets*, 98(5):7871–7885.

[Von Herzen et al., 1983] Von Herzen, R., Francis, T., and Becker, K. (1983). In-situ large scale electrical resistivity of the oceanic crust, hole 504b. *Init. Reps of DSDP, eds Cann et al.*, 69:237–244.

[Wolfgram et al., 1986] Wolfgram, P., Edwards, R., Law, L., and Bone, M. (1986). Polymetallic sulfide explorations on the deep sea floor: The feasibility of the mini-moses experiment. *Geophysics*, 51(9):1808–1818.

[Yang and Tseng, 1992] Yang, C. and Tseng, H. (1992). Topographic responses in magnetometric resistivity modeling. *Geophysics*, 57(10):1409–1418.